Acta Materialia 265 (2024) 119604

Contents lists available at ScienceDirect

Acta Materialia

journal homepage: www.elsevier.com/locate/actamat

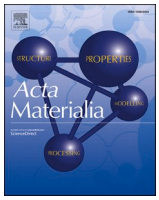

Ambient grain orientation imaging on complex surfaces

Alistair Speidel [a,*], Ivan Bisterov [a], Shamraze Ahmed [a], Adam Thomas Clare [a,b]

[a] Faculty of Engineering, University of Nottingham, Jubilee Campus, Nottingham, NG7 2GX, UK
[b] School of Engineering, Department of Mechanical Engineering, University of British Columbia, 2054-6250 Applied Science Lane, Vancouver, BC, V6T 1Z4, Canada

ARTICLE INFO

Keywords:
Materials characterization
Grain orientation mapping
Electrochemistry
Ambient condition

ABSTRACT

Crystal orientation imaging is generally confined to the laboratory, typically following destructive sectioning, with most current techniques reliant on electron-material interactions that require a vacuum. This information is gathered in a manner that requires careful planning, however a more desirable approach would allow the manufacturer to acquire this data non-destructively at the point of manufacture, with little or no time penalty. We show that coupling a numerically controlled etching method to topographical data processing can be used to spatially map grain orientations over planar and non-planar surfaces. Our method allows the construction of large area orientation maps (≈400 mm^2) in agreement with electron backscatter diffraction datasets. We have characterized spatial and angular resolution limits for the technique, which are correlated to length scales of microscale etch surfaces and our ability to measure their geometries. This approach has the potential to augment materials processing technologies, where resultant microstructures require strict control in order to guarantee through-life integrity.

1. Introduction

The ability to perform microstructural imaging across parts in a less destructive and lower intervention manner is a common theme in the study of materials processing and high value manufacturing. The functional performance, including mechanical [1,2], electrical [3,4], magnetic [5], and thermal properties [6] of parts manufactured from polycrystalline materials is determined by microstructural properties of grains, for example the geometric characteristics like size and shape, their absolute and relative orientations, and the nature of the grain boundaries that separate them.

The capacity to measure these within a production line, or better still within a machine tool, opens new possibilities to extract materials data on the factory floor. This presents opportunities to extract more value from engineering products through understanding their limitations during manufacture. This is especially important given the drive towards more complex materials [7] and new manufacturing methods like additive manufacturing from which resulting microstructures may be more challenging to predict and control [8,9].

Crystallographic orientation mapping is typically performed using diffraction-based methods, like electron backscatter diffraction (EBSD) [10,11]. Such is the ubiquity and importance of EBSD throughout materials science, the technique itself is practically synonymous with orientation mapping. In EBSD, electrons from a primary beam scatter elastically from atomic nuclei within a crystalline sample and diffract through near surface lattice planes. The projection of these backscattered electrons onto a detector creates patterns (Kikuchi bands), which correlate to the alignment of the lattice relative to the detector [12]. While the resulting information is invaluable to engineers and materials scientists alike, the application of EBSD is limited by the time and cost of analysis, while also requiring small areas of flat and highly polished surfaces that often must be destructively sectioned from a larger part.

As such, there is interest to acquire orientation information rapidly *ex-vacuo* to democratize high level measurement within manufacturing, where techniques must rely on anisotropic interactions, for example between an energy source or reaction and the microstructure. Alternate diffraction methods can be performed under ambient conditions, such as X-ray diffraction contrast tomography (DCT) [13], which can allow the non-destructive three-dimensional evaluation of materials. This capability allows operando observation of metallurgical phenomena of interest such as solidification and grain growth [14], while adaptions have increased its practicality for use in the laboratory [15,16]. DCT ultimately relies on the diffraction and transmission of X-rays through a sample, which means there are limits to sample size (e.g. mm scale), especially for dense materials with high X-ray scattering cross sections.

* Corresponding author.
E-mail address: alistair.speidel@nottingham.ac.uk (A. Speidel).

https://doi.org/10.1016/j.actamat.2023.119604
Received 18 May 2023; Received in revised form 8 December 2023; Accepted 12 December 2023
Available online 13 December 2023

Different methods not reliant on diffraction are emerging to image orientations over large surface areas. For example, spatially resolved acoustic spectroscopy (SRAS) in which the energy source is a probe laser [17,18], Raman orientation mapping [19], and selective chemical [20] and electrochemical etching [21] that can unveil specific characteristic etch facets. Analyzing the relative orientations of these etch facets forms the basis of directional reflectance microscopy (DRM) [22,23], as well as topographic approaches to microstructural characterization [24,25]. In addition, polarized light microscopy (PLM) is an established metallurgical analysis tool that has been applied for decades to observe optically anisotropic materials, where recent advances have focussed on the development of new computation approaches to map local optical axis orientations in hcp materials [26]. PLM is fundamentally limited to optically anisotropic materials, which excludes cubic materials that represent a significant proportion of the matrix forming alloys that are used in modern engineering applications. As such, recent studies have combined chemical etching to generate anisotropic surface features with PLM to allow full orientation mapping in cubic materials [27]. Optical microscopic imaging is limited by a shallow depth of field; practically this limits its application to flat surfaces. There remains a requirement for rapid surface sensitive methods that are robust to surface geometry.

In this study, a topographic approach to extracting orientation information was developed as topography measurement tools must be robust to complex surface geometries (i.e. non-planar surfaces). Assuming the effective 'wavelength' (form) of the macroscale surface geometry is significantly greater than the microscopic length scales of the characteristic etch facets, a resulting orientation extraction routine based on direct topography analysis should, in principle, be robust to the surface form. Even for smaller scale surface geometries that approach the length scales of etch facets, carefully selected [28] wavelength filtering could be applied to overcome this effect. Topography measurement routines are often already implemented as quality control within certain current high-value production processes [29] and thus could be readily integrated with a numerically controlled etching approach to enable rapid automated mass microstructural imaging of parts on the production line [30]. This approach will be particularly relevant for high symmetry materials (e.g. order ≥ 24), such as cubic and hcp structures, which typically form characteristic etch facets that can readily be correlated to discrete lattice plane families. These crystal classes encompass the majority of current matrix forming engineering alloys.

Typically, etching is performed by swabbing or immersion in acidified etchants. This is often a manual process where removal volumes are influenced by exposure time, etchant concentration, and temperature. Electrochemical reactions can offer a high level of control, where removal is proportional to the quantity of charge passed. Furthermore, numerically controlled electrochemical jet processes offer selective etching using non-hazardous electrolytes [31], can be operated within a production and line independent of sample geometry [32], and have been applied towards surface preparation in materials characterization of conventionally rolled [33,34], and additively manufactured materials [35].

In this study, we have simulated orientation dependent etch responses for Al, which we have validated against etched surfaces of single crystal specimens. We have subsequently verified the orientation outputs against data acquired from a commonly used polycrystalline sample of a commercial Al-alloy (6082) using EBSD, to generate spatially resolved orientation maps. Al-alloys were selected as the subjects because they are a challenging subject for conventional high-fidelity methods like EBSD, where the low atomic number generates relatively low signal counts, increasing acquisition times and where Al-alloy lattices are relatively soft and deform readily, further complicating diffraction pattern acquisition. Furthermore, the topographic response to etching has been previously characterized and is highly selective, with the resulting surfaces perpendicular to the ⟨001⟩ crystallographic directions [36]. The response was also validated for a commercially pure Ni sample, where the resulting surfaces are perpendicular to the ⟨111⟩ crystallographic directions.

2. Materials and methods

2.1. Materials and topography preparation

Etch response was validated against high purity (> 99.9%) single crystal specimens (± 2°) of Al (10.0 × 10.0 × 1.0 mm), corresponding to the principle cubic orientations [100], [110] (Alineason, Germany), and [111] (MTI Corporation, USA). A commercial grade Al-alloy (6082) and commercially pure Ni was also processed to demonstrate large-area mapping capability. All samples were etched using an electrochemical jet machining (EJM) apparatus, previously described [33].

All samples were etched using a pH neutral and non-hazardous NaCl electrolyte (2.5 M, $\sigma = 152.2 \pm 0.1$ mS/cm at 22.3 °C). Single crystal samples were etched using a cylindrical nozzle ($\varnothing = 0.51$ mm), while the commercial 6082-alloy was etched using rectangular slot jet (10.0 × 0.3 mm), which allows large area etching [33] and electrochemical milling [37]. Surface current density, J, is a primary factor affecting the development of etch facets [38]. This can be approximated by the ratio between applied current, I, and planar nozzle area, A. Informed by previous work [25], an identical current density ($J = 0.5$ A/mm^2) was used to process all samples. $I = 0.1$ A was applied through the cylindrical jet ($A = 0.20$ mm^2) and $I = 1.5$ A through the large area slot jet ($A = 3.00$ mm^2), respectively. Inter-electrode gap (IEG) distance was maintained at 0.5 mm throughout processing. Potential was left to float depending on IEG resistance, R, but the range was broadly consistent for all operations (16 – 21 V).

Small pockets (3 × 3 mm) were etched into the single crystal samples using a serpentine toolpath at a nozzle feed rate, ν_f, of 0.2 mm/s. Large areas (20 × 20 mm) were etched using the slot jet ($\nu_f = 0.4$ mm/s) in a unidirectional toolpath, to account for any asymmetry between the two plates of the electrified nozzle. Complex surfaces were generated by varying the feed rate between 0.13 and 0.4 mm/s to vary removal. Jet velocity, ν_j, was maintained at 16.4 ± 0.1 m/s for the cylindrical jet and 5.1 ± 0.1 m/s for the slot jet. Samples were rinsed in deionized water after etching and cleaned in an ultrasonic bath, before drying.

A sample of the same Al-alloy was processed using a continuous wave laser (λ = 1060–1080 nm) at a power of 1.5 kW with a spot size of 0.3 mm. Three single tracks were written onto the surface varying the laser scanning speed between each track (20, 60, 100 mm/s). The sample was then etched with the jet as above and analyzed without further preparation.

2.2. Constructing topography intensity profiles

This section details the construction of topography intensity profiles (TIPs) from facet normal vectors, whose direction can be described by spherical coordinates (Fig. 1a); these are characteristic for a given facet orientation. These can be both simulated computationally and extracted from surface topography data. Considering the simulated TIP, an ideal geometric model was used. For etched Al, etch facets generally follow the ⟨001⟩ directions, i.e. normal to the faces of a cube, which is understood to result from the stability of the native oxide film [36,39]. For Ni and many other cubic materials, these slow etch directions generally follow the densely packed {111} planes, normal to the faces of a regular octahedron and the dual polyhedron of the cube. The grain-specific contrast apparent in the 'macroscale etch' shown in the optical micrograph in Fig. 1b results from these characteristic etch topographies at the microscale (Fig. 1c).

As the surface normal of a given facet can be directly correlated with a crystallographic direction, a methodology to extract crystallographic orientation can be proposed – if the topography can be accurately measured. Vectors, which correspond to the facet normals, or vertices, can be subjected to any predefined sequence of rigid body rotations

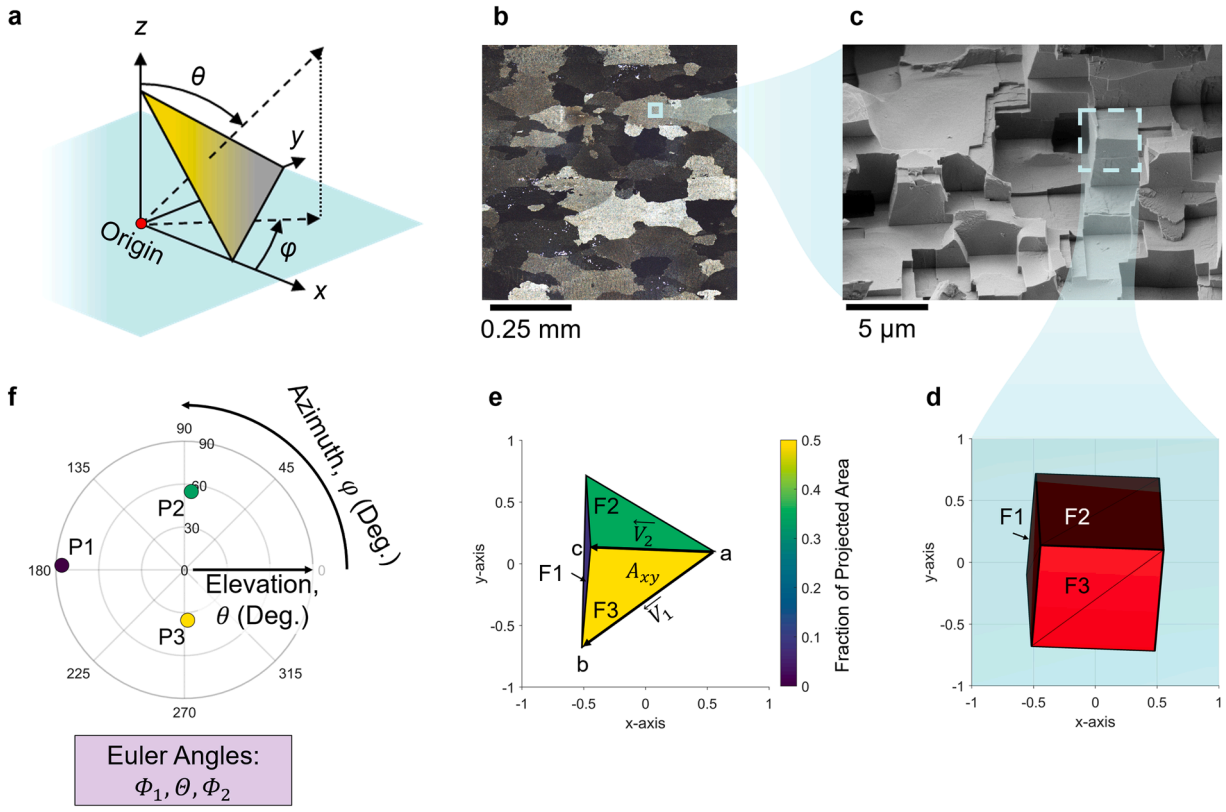

Fig. 1. From surface normals to crystallographic orientation. a) Angular representation used throughout the study to describe face normal vectors, where elevation, θ, is measured from the polar axis, z, and the azimuthal angle, φ, is measured anticlockwise from the x-axis. b) Optical micrograph of a typical 'macro-etched' surface of an Al-alloy showing grain contrast and c) a secondary electron micrograph of the characteristic microscale etched surface topography. d) Topography response can be predicted for any arbitrary Euler angles and matched against measured surface topography, shown with a geometric model triangulated from cubic vertices after matrix rotations. This can be performed directly with orthogonal vectors. e) The relative areas of the faces in the viewing (xy) plane can indicate a scaled peak intensity factor. Area (A_{xy}) is the vector cross product between $\overrightarrow{V_1}$ and $\overrightarrow{V_2}$, shown for face 'F3' projected onto the xy-plane. f) A predicted topography intensity profile (TIP) of the peak maxima for the arbitrary orientation shown in d), where peak colour is scaled to the fraction of the projected area. For Al, this is essentially a (100) pole figure. Euler angles can be extracted from arbitrary surface topographies by comparing measured and simulated TIPs. (For interpretation of the references to color in this figure legend, the reader is referred to the web version of this article.).

about the *x*, *y*, and *z* axes from a fixed point of origin Eqs. (1)–((3), respectively).

$$RX = \begin{bmatrix} 1 & 0 & 0 \\ 0 & \cos\theta & -\sin\theta \\ 0 & \sin\theta & \cos\theta \end{bmatrix} \tag{1}$$

$$RY = \begin{bmatrix} \cos\theta & 0 & \sin\theta \\ 0 & 1 & 0 \\ -\sin\theta & 0 & \cos\theta \end{bmatrix} \tag{2}$$

$$RZ = \begin{bmatrix} \cos\theta & -\sin\theta & 0 \\ \sin\theta & \cos\theta & 0 \\ 0 & 0 & 1 \end{bmatrix} \tag{3}$$

Fig. 1d shows a cubic system subjected to arbitrary rotations such as to bring the model into apparent agreement with the crystallite indicated by the blue dashed box in Fig. 1c. Spherical coordinates corresponding to the azimuthal angle (direction), φ, and the polar angle, θ, corresponding to the elevation (slope) of an exposed facet can be calculated from the model normal vectors through Eqs. (4) and (5), respectively. The radial distance, *r*, is taken as 1 for unit vectors here.

$$\varphi = atan2\left(z, \sqrt{x^2 + y^2}\right) \tag{4}$$

$$\theta = atan2(y, x) \tag{5}$$

Relative intensities of the azimuthal and polar angles associated with a given facet can be predicted by assigning a scale factor related to the area of the facet projected onto the viewing plane (*xy*-plane) (Fig. 1d). For triangulated features, the projected surface area in the *xy*-plane, A_{xy}, can be calculated by the vector cross product (Eq. (6)):

$$A_{xy} = \frac{1}{2}\left|\overrightarrow{V_1} \times \overrightarrow{V_2}\right| \tag{6}$$

where $\overrightarrow{V_1}$ is the projection of the vector between point *a* and *b* on the *xy* plane, and $\overrightarrow{V_2}$ is the projection of the vector between point *a* and *c* on the *xy* plane (Fig. 1e). This is grounded by the fact optical topographic measurements are line-of-sight with a defined viewing plane, such that high gradient surfaces will contribute a lower fraction of the projected measurement area than flat surfaces. Peak positions corresponding to facet normals can be described by spherical coordinates projected onto an abstract sphere. Here, the azimuthal angle is measured anticlockwise from the *x*-axis of the microscope (and thus the topography data), while the elevation is measured from the *z*-axis (zenith).

From this, a topography intensity profile (TIP) can be predicted (Fig. 1f), which is the topography analog of a directional reflectance profile [22,23]. The TIP is the analog to other stereographic vector projections such as interfacial normal distributions [40] and pole figures. For the Al etch facets, the TIP is essentially a stereographic projection of the (100) pole figure. Azimuth is represented on the polar axis of the TIP, while the elevation is marked by the radial position. Peak color in Fig. 1f is scaled to the projected area of the surface features, such that the relative intensities of the peaks can be approximated.

A TIP can also be constructed from collected surface topography data Section 2.3) by applying Eqs. (4) and ((5) over the data in a pixelwise manner. Areas of high intensity in the resulting TIP correspond to aggregations of similarly oriented etch facets. By applying this approach, a simulated TIP can be predicted for any arbitrary crystallographic orientation and the relative peak positions can be compared with a TIP acquired from etched surface topography data to infer local crystallographic orientation. Heat maps presented in this study are colored with the 'Viridis' perceptually uniform colormap [41].

2.3. Characterization

SE micrographs were acquired using a Philips XL-30 secondary electron microscope, while electron backscatter diffraction (EBSD) data were acquired in a Helios G4 PFIB microscope, using an Oxford Instruments Symmetry CMOS detector.

Surface height (topography) data was acquired using a Zygo NexView coherence scanning interferometer (CSI) with a 50x Mirau lens with an effective field of view (FOV) of 173 × 173 μm (≈0.173 μm/pixel) [42]. Where surface height is presented in this study, it is measured from the CSI topography data and offset such that the minimum value of the point cloud is the 0 μm value. Large area maps were stitched from multiple FOVs, where each FOV was acquired with a 20% data overlap to aid stitching. Topography data was filtered to remove surface form by a third order polynomial prior to subsequent processing. Aliasing artefacts that result from the pixelwise topography data were removed by Gaussian filtering ($\sigma = 0.75$) prior to data processing, detailed in Supplementary Fig. 1.

EBSD and topography datasets were overlaid for pixelwise comparison by applying a 2D image transformation to the EBSD dataset. This transformation was calculated from selected easily identifiable features-in-common (control points) between the two datasets, such as triple points extracted from the grain boundary data (Supplementary Fig. 2). These additional steps were undertaken using the inbuilt MATLAB functions fitgeotform2d.m and imwarp.m. This transformation was applied to the spatial coordinates of the EBSD dataset, but not the EBSD Euler angles.

3. Results and discussion

3.1. Spatial resolution

Assuming the microscope can transmit accurate surface data at the length scale of the etch facets, several challenges to elucidating the spatial resolution of the method remain. Firstly, a process reliant on aggregate measurements of many similarly oriented etch facets will be vulnerable to sampling smaller areas, where there are fewer facets per measurement area. Secondly, the size of the etch facets may affect the spatial resolution limit; a corollary of which is that a spatial resolution limit is likely to be somewhat dependent on the underlying crystalline orientation. The presence of secondary phases or precipitates within the grains and at the boundaries is also likely to disrupt the formation of etch facets and obscure analysis. The correlation between the dominant peak predictions and etched topography was appraised for high purity single crystal samples, representing an ideal material with an etch response unencumbered by material heterogeneity or precipitates that exist within most commercial Al alloy grades.

To understand the effect of orientation on the generation and size distributions of etch facets, single crystal samples were etched at one current density (0.5 A/mm^2). Size variability of facets resulting from electrochemical etching has been previously shown to be dependent on the applied current density that affects mass transport phenomena in the removal zone [25], however this aspect is not challenging to control using electrochemical jet methods. Facet areas were characterized by motif analysis [43] from topographic datasets (173 × 173 μm) for each of the single crystal samples and shown in the boxplots in Fig. 2a. SEM micrographs of the respective etched surfaces of the equivalent single crystal samples are shown in Fig. 2b–d, along with synthetic surfaces (Section 2.2) that show the major and minor expected surface normal vectors for each sample (Fig. 2e–g), corresponding to their relative surface areas. Facets that evolve over the [100]-oriented sample on etching have marginally greater areas (interquartile range: 5.4–27.1 μm^2) than either the [110] or [111]-oriented specimens (0.5–12.4 μm^2 and 1.5–9.2 μm^2, respectively) at identical etching parameters. Furthermore, the area of the largest etch facet on each sampling area is

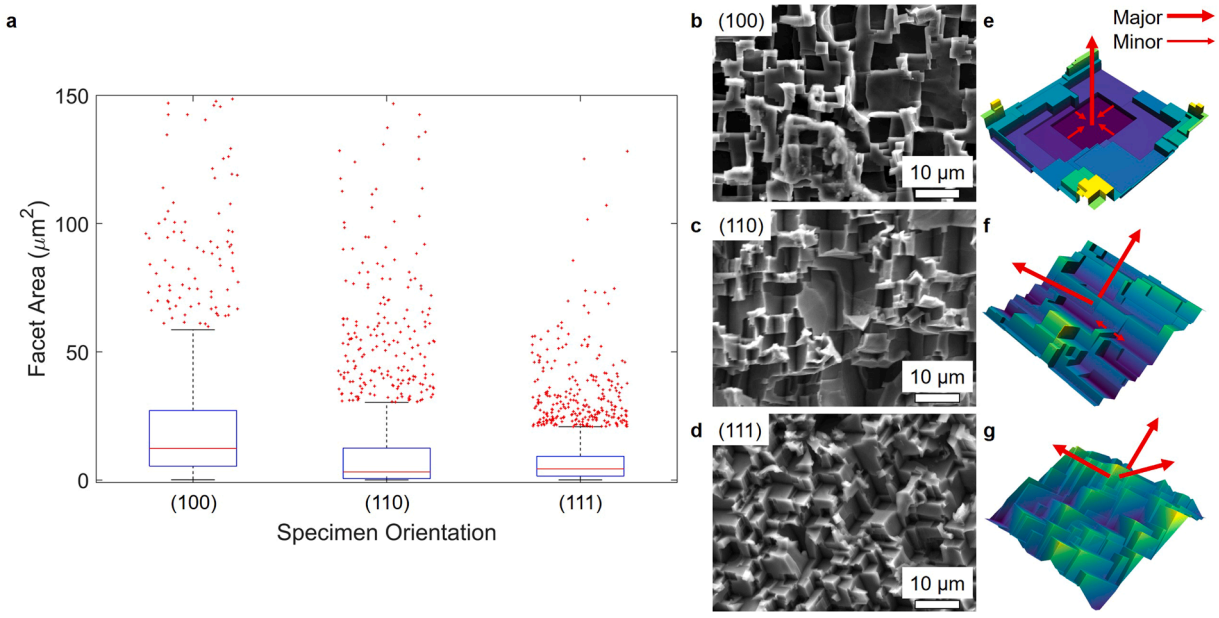

Fig. 2. Facet size is dependent on the underlying crystalline orientation. a) Facet area boxplots for the single crystal samples etched at 5.0 A/mm^2 over a 1-megapixel surface area (173 × 173 μm). Red crosses are outliers beyond 1.5 times the interquartile range. Secondary electron micrographs of b) [100]-oriented, c) [110]-oriented, and d) [111]-oriented single crystal surfaces after etching. e-g) Schematic surfaces representative of etched [100], [110], and [111]-oriented crystals (respectively) showing the major and minor surface normal vectors expected, indicated by arrow thickness. Population sizes in (a): n[100] = 1071, n[110] = 2846, n[111] = 3972 (For interpretation of the references to color in this figure legend, the reader is referred to the web version of this article.).

significantly greater for the [100]-oriented sample (1481 μm^2) compared with either the (110)-oriented (686 μm^2), or the [111]-oriented surfaces (128 μm^2). Therefore, a given sampling area of material that is oriented vicinal to [100] will have fewer etch facets. This is reflected in the facet populations over the same surface area tested here (≈ 0.03 mm^2): n[100] = 1071, n[110] = 2846, n[111] = 3972.

A situation where relatively few etch facets occur within a given sampling area will present challenges to lattice vector acquisition and orientation extraction routines (Section 3.2). As an extreme example, consider a single [100]-oriented facet with an area > 1000 μm^2, a statistical anomaly in this study, but possible. If a sampling region were to fall within the area of one facet, this would only allow the resolution of a single surface normal vector. This is inadequate to fully resolve the orientation of the underlying crystal. However, this case is technically possible, albeit unlikely, where the effective measurement step size is < 30 μm.

While it is unsurprising that facet areas are greater when the slow etch crystallographic directions are aligned normal to the sample surface and thus the dissolution front, understanding the extent of this relationship is important to elucidating any effect of the underlying orientation on the spatial resolution. However, we have previously shown that the length scale of the etch facets is sensitive to easily adaptable parameters like the applied current density of the electrolyte jet, such that it is likely possible to tune the size of the etch facet to the microscope resolution [25], the caveat being prior knowledge of the particular alloy is required.

In this study, we assessed the effective spatial resolution for each principle orientation by sampling surface areas of etched single crystal over several orders of magnitude (10 – 250,000 μm^2), comparing dominant topographic peaks to those predicted by the forward model. Relative predicted peak locations from the forward model are shown in Fig. 3a–c for the principle [100], [110], and [111] orientations, after manipulation according to the listed Euler angles (Φ_1, Θ, Φ_2), and colored according to expected area fraction for each peak. Absolute peak coordinates for the single crystal specimens are dependent on the in-plane (xy) rotation of the crystal lattice with respect to the sample orientation, which is unknown until directly observed, for example through EBSD, or etching and data acquisition. A perfect [100]-oriented

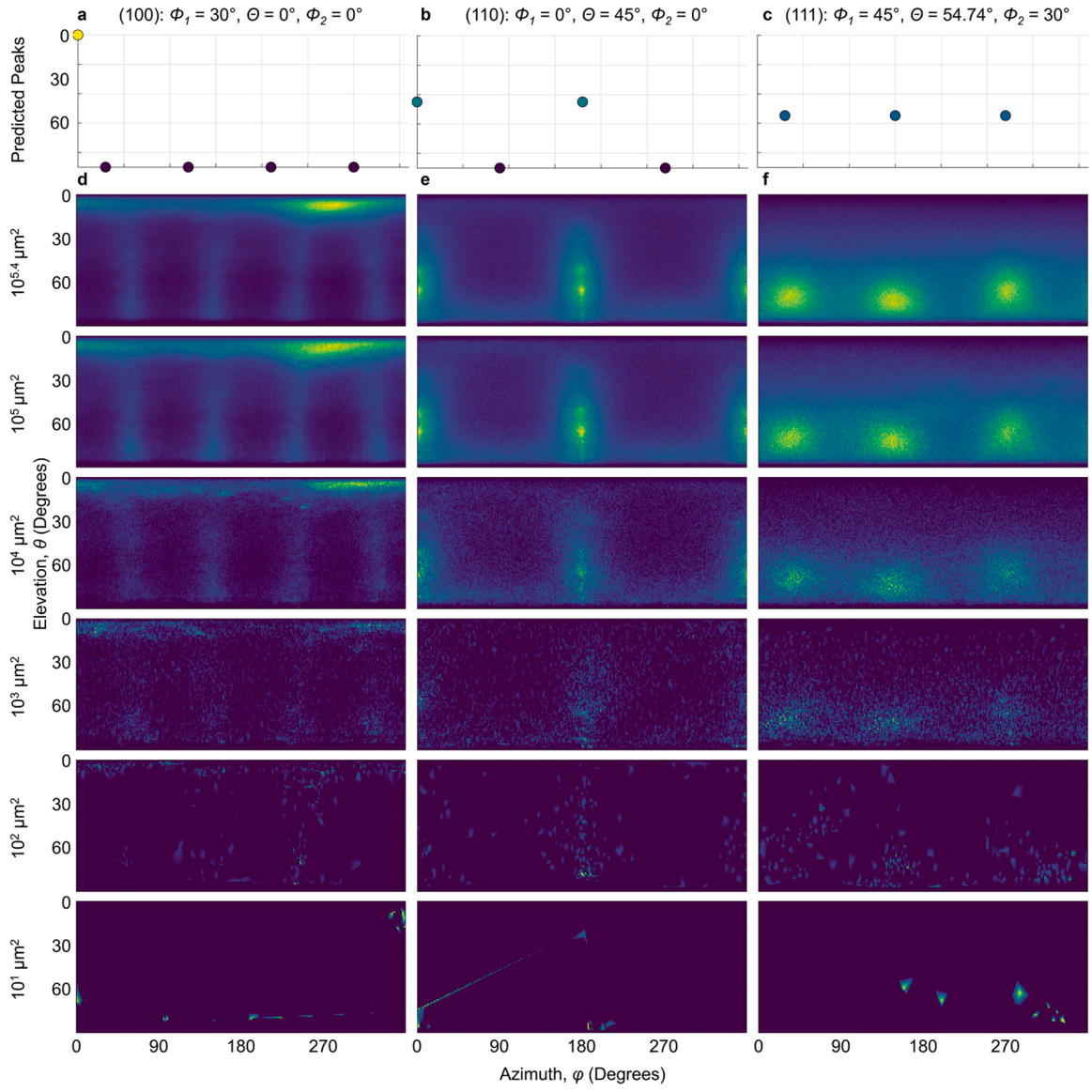

Fig. 3. Degradation of signal upon decreasing sampling area. Predicted and measured cartesian topography intensity profiles over a range of sampling areas (250,000–10 μm^2) for single crystal samples a) [100], b) [110], and c) [111]. Topography datasets subjected to Gaussian filtering (σ = 0.75) prior to extraction of spherical coordinates. x-axis (0–360°) and y-axis (0–90°) are consistent throughout the figure (For interpretation of the references to color in this figure legend, the reader is referred to the web version of this article.).

etched Al single crystal would be expected to return a high intensity peak at low elevation ($\theta = 0°$), with four minor high elevation peaks separated by $\varphi = 90°$ (Fig. 3a). Intuitively, the azimuthal direction of the high intensity peak becomes indeterminate as the elevation approaches zero. A [110]-oriented sample would be expected to return two dominant peaks at $\theta = 45°$, separated by $\varphi = 180°$ (Fig. 3b). Minor peaks at high elevation, corresponding to vertically aligned {100} planes will be observable if the microscope is capable of measurement at these length scales; these features can be seen in the SEM micrograph in Fig. 2c. A [111]-oriented sample would be expected to return three dominant peaks at $\theta \approx 54.74°$, separated by $\varphi = 120°$ (Fig. 3c).

TIPs constructed from the acquired topography data through Eqs. (4) and (5) are shown in Fig. 3d-f for the [100], [110], and [111]-oriented single crystals, respectively, after Gaussian filtering ($\sigma = 0.75$). Sampling area decreases from the top row to the bottom ($10^{5.4} - 10^{1}$ μm^2), and thus the number of processed pixels for these surface areas decreases over this range (8353,000–334, 0.173 μm step size). This is reflected in a signal drop down each column.

TIPs are broadly in agreement with the predicted peak locations; high elevation peaks in the [100]-oriented sample are dilated over the entire elevation range due to the data filtering (Section 3.1), while the minor predicted peaks expected in the [110]-oriented sample appear as a continuous high-angle band over the entire azimuthal range. Peaks are unresolvable at sampling areas $< 10^4$ μm^2 indicating a step size limit for orientation resolution of approximately 100 μm with the current optical interferometer at this etching current density. Below this, signal counts are low, challenging the extraction of spherical coordinates describing the surface normal vectors. At the smallest sampling area tested (10 μm^2, 3.16 μm lateral step size), the analysis region is likely to fall over a small number of etch facets and the data is likely unrepresentative.

While facet sizes of commercial alloys are unlikely to be equivalent to high-purity single crystal samples that have no grain boundaries and precipitates, general facet area relationships, e.g. (100) > (110) ≈ (111), are likely to hold true for most Al matrix polycrystals given the strong etch selectivity. Sampling areas of 12,100 μm^2 (110 μm step size) were therefore used for orientation mapping in this study (Section 3.3) and a sliding window approach along the *x* and *y* axes was applied to oversample the data with a 55 μm step to enable super-resolution mapping.

3.2. Orientation extraction: a study in single crystals

An orientation, **G**, can be described by three successive (or

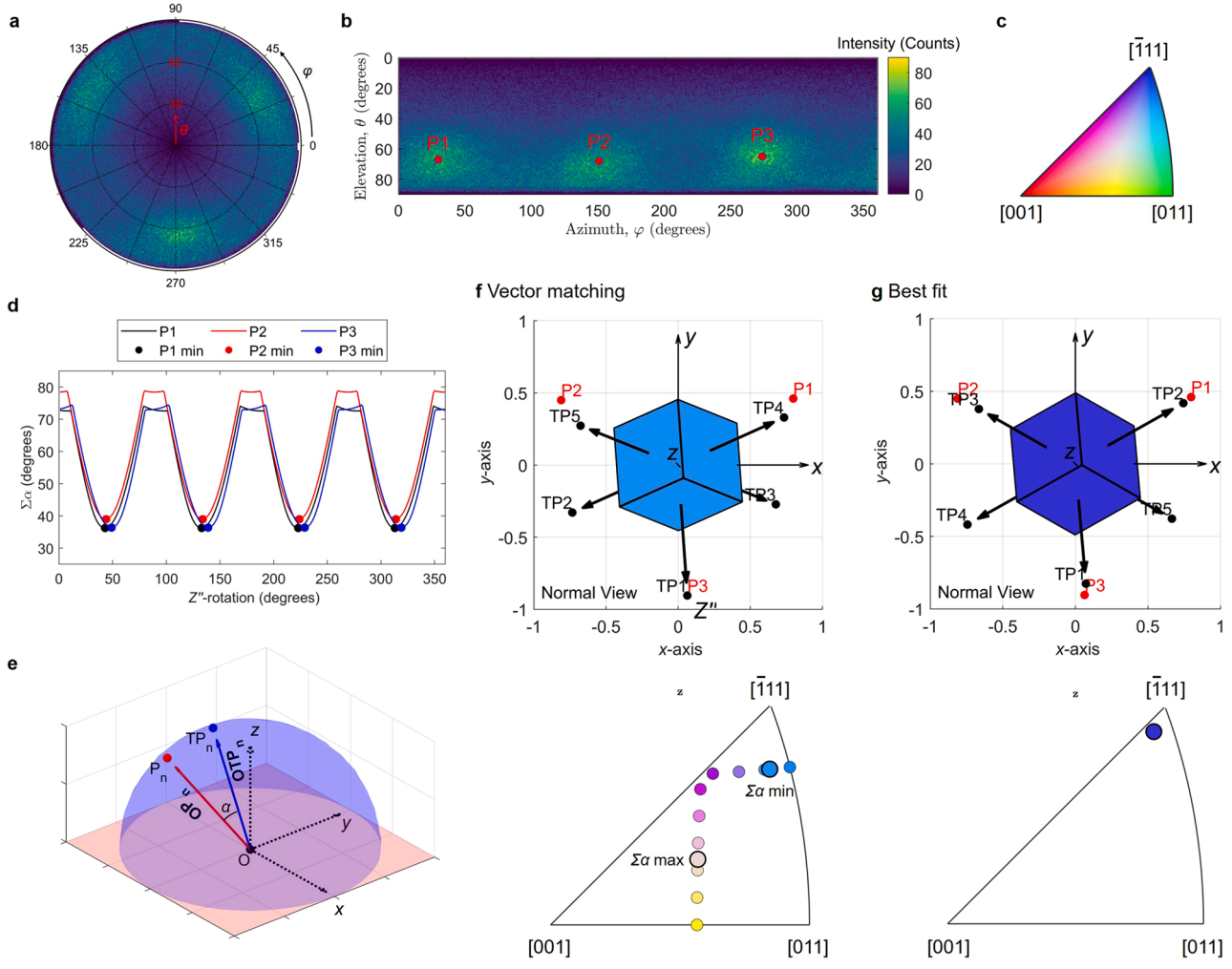

Fig. 4. From topography data to orientation prediction. a) Topography intensity profile (TIP) of etched [111] single crystal Al showing relative intensity of surface azimuths and elevations, from which local maxima can be extracted, arbitrarily named P1 – P3 (b). c) Standard HSV coloring used to represent inverse pole figures throughout this study. d) The sum of angular separations, Σα, for the [111]-oriented single crystal across the Z''-rotation range (1 - 360°). e) The angular difference, α, between a given data peak, Pn and a peak predicted from the model TPn can be calculated from the unit normal vectors OPn and OTPn, where O is the origin. f) Model output of the vector matching approach colored according to (c) with associated IPF tracing the orientations (z-reference) across the Z''-rotational range (5° increments). g) Model output of the best fit method colored according to the associated IPF (For interpretation of the references to color in this figure legend, the reader is referred to the web version of this article.).

composed) rotations with respect to a specified reference direction, **r**. Here, we apply intrinsic rotations about the reference *z*-axis, Φ_1, about the new *Y'*-axis, Θ, followed by another rotation, Φ_2, about the new *Z''*-axis (Matthies notation), such that:

$$\mathbf{G} = Rz(\Phi_1)Y'(\Theta)Z''(\Phi_2) \tag{7}$$

The lattice direction, **h**, can be computed by Eq. (8) and plot to an inverse pole figure (IPF). This final step was performed using the MTEX add on for MATLAB [44]:

$$\mathbf{h} = \mathbf{G}^{-1}\mathbf{r} \tag{8}$$

Each identified peak in the topography data is associated with an aggregation of etch facets that, for Al-alloys, aligns with $a\langle 100\rangle$ direction. To solve the inverse problem, i.e. elucidating possible manipulations of the cube from topographic height data, a TIP must be constructed (Fig. 4a), shown here for a [111] single crystal sample (173 × 173 μm, ≈ 0.03 mm^2). Spherical coordinates can be extracted from this data (Fig. 4b), for comparison with the geometric model. This routine is sensitive to the method used to extract coordinate positions. All inverse pole figures (IPFs) are displayed with HSV coloring (Fig. 4c). Comparisons between surface data and the forward model are made by assessing the angular separation, α, between surface data vectors ($\mathbf{OP_n}$, where O is the origin) and the topography profile vectors ($\mathbf{OTP_n}$) that are output from the model (Fig. 4e), calculated from Eq. (9).

$$\alpha = \cos^{-1}\left(\frac{\overrightarrow{OP_n}\cdot\overrightarrow{OTP}}{\left|\overrightarrow{OP_n}\right|\left|\overrightarrow{OTP}\right|}\right) \tag{9}$$

We used two approaches to extract Euler angles from the topography data; a vector matching routine, and a best fit routine (brute force method). In the vector matching route, rotations corresponding to the first two Euler angles can be taken as the spherical coordinates (φ, θ) for a given data point (P_n). Performing these sequential rotations by Φ_1 and Θ about the *z*- and *Y'*-axes respectively matches a simulated topography profile (TP) vector from the model ($\mathbf{OTP_n}$, where O is the origin) with the selected data point (P) (Supplementary Fig. 2). Any subsequent rotation about the *Z''*-axis satisfies this criterion and so to acquire a value for the final Euler angle (Φ_2), a fitting routine is used. Here, the vector set is rotated about the *Z''*-axis over the whole Φ_2 range (0 - 360°, in increments of 1°) (Supplementary Video 1).

We take the value of Φ_2 to be the rotation that leads to the minimum sum of the angular separations, $\Sigma\alpha$, between the data point vectors ($\mathbf{OP_n}$) and the predicted topography profile vectors ($\mathbf{OTP_n}$), essentially returning the closest match with the ideal geometric response. As the surface topography data possesses artefacts (Supplementary Fig. 1), and due to natural variation in the geometry of etch facets, there is a separation between the data points and the predicted topography profile that results from an orthogonal vector set.

This is performed for each of the data points (e.g. 'P1' – 'P3'), over the entire *Z''*-rotation range and the $\Sigma\alpha$ values are shown in Fig. 4d for the [111]-oriented crystal surface analyzed in Fig. 4a, where the $\Sigma\alpha$ minima are marked for each matched data point. In this example, Φ_2 is closely grouped independent of which data point is matched by the model (P1: 43°, P2: 44°, P3: 49°). There are equivalent minima at 90° separations, which result from the C_4 rotational symmetry of a cube around one fixed axis, i.e., the practical Φ_2 range is 0–90° The set of Euler angles which minimizes $\Sigma\alpha$ is selected as the orientation, $\mathbf{G}(\Phi_1, \Theta, \Phi_2)$, with respect to a reference vector, **r**, for mapping and comparative studies.

Exemplar rotations around the fixed *Z''*-axis are plot onto the IPF in Fig. 4f (increments of 5°). The orientation shift upon rotation around the fixed Z''-axis can be traced across the IPF. The orientations corresponding to the minimized and maximized $\Sigma\alpha$ values are shown as enlarged points on the IPF and the vector matched model output (colored according to the minimized $\Sigma\alpha$, Fig. 4f).

A best fit approach, in which all possible Euler angles are fit to the surface data coordinates was also appraised. As there are infinite orientations, we used arbitrary 1° increments across the Φ_1, Φ_2 range (1 - 360°), and Θ range (1 - 90°). The resulting minimized $\Sigma\alpha$ model output is shown in Fig. 4g, colored according to the corresponding IPF. This returns an orientation that is close to the [111] single crystal reference specimen, although the routine is more computationally expensive than vector matching. This was accelerated by running a coarse fitting pass (6° increments) to define a primary Euler angle set, prior to a refinement operation (± 6° from Φ_1, Θ, Φ_2). For ranges tested (Φ_1 and Φ_2: 1–360°, Θ: 1–90°), this represents a significant reduction in the number of calculated orientations (11,644,000 to 56,200) and thus the computation time.

The minimized $\Sigma\alpha$ is similar for both the vector matched (36.6°) and best fit (35.6°) approaches. This is indicative of the sum of the differences between extracted elevations from the surface data (θ: P1 = 67°, P2 = 67°, P3 = 65°) and the ideal slope angle for a [111]-oriented Al single crystal ($\tan^{-1}\frac{1}{\sqrt{0.5}} \approx 54.7°$).

The accuracy of the vector matching approach is sensitive to the elevation, θ, of the peak coordinate, which dictates the *Z''*-axis about which the model vectors are rotated to determine Φ_2. This sensitivity appears to reduce where there are more peaks with which to compare the model. This indicates that the accuracy, when applying the vector matching approach, is dependent on the underlying orientation.

[100] and [110]-oriented single crystal specimens possess a different number of characteristic topographic peaks, which is intuitive as the topography profile is directly correlated to the (100) pole figure for each orientation. Topography profiles are shown in Fig. 5a and b for [100] and [110]-oriented specimens; five peak coordinates were extracted from the [100]-oriented and two from the [110]-oriented specimens. The corresponding angular difference plots over the *Z''*-rotation range acquired from the extracted surface coordinates are shown in Fig. 5c and d. The high amplitude *Z''*-rotational trace in Fig. 5c ('P5') corresponds to vector matching with the high-intensity low angle peak (Supplementary Video 2). The extracted orientations from all tested single crystals calculated by both routines are plot onto the IPF (see Fig. 4 for reference to the [111]-oriented sample), while the corresponding lattice orientation is visualized for both [100] and [110]-oriented specimens in Fig. 5e–h. Vector matching returns an orientation that is close to the single crystal orientation for the [100]-oriented data (Fig. 5e), but not for the [110]-oriented data (Fig. 5g).

The best fit approach matches the orthogonal vector set giving equal priority to each topographic peak extracted from the TIP regardless of intensity or peak position. This will not necessarily lead to the best indexing result. One such scenario is indicated in Fig. 6, of an etched single crystal region of a larger 6082-alloy polycrystal. In this case, the grain of interest is oriented vicinal to [100] (Fig. 6a). In the associated TIP (Fig. 6b) one 'major' high-intensity peak is returned at a well-defined low elevation, θ, (see also Fig. 5a), but where the azimuthal angle, φ, is poorly defined. In addition, multiple low-intensity 'minor' peaks will be returned with defined φ, but with poorly defined elevations resulting from both the banding in the TIP, and the physical limits of line-of-sight metrology at high elevation angles. In this case, vector matching with the low intensity peak (through rotations around the *z* and *Y'*-axes) will define a 'tilt' axis of the crystal relative to the microscope. Subsequent rotations around this *Z''*-axis will allow calculation of the angular minima between the model and topography vectors, exploiting the well-defined azimuthal angles and separations of the 'minor' peaks. The inverse pole figures for the **z, y**, and **x** directions are shown in Fig. 6c for the extracted Euler angles resulting from EBSD (enlarged), and both the vector matching (VM), and best fit (BF) approaches. There is additional uncertainty in the IPF-y and x plots resulting from the manual alignment of the sample in both the SEM in which the EBSD data was acquired, and the optical microscope.

This will typically only return a better result than the best fit

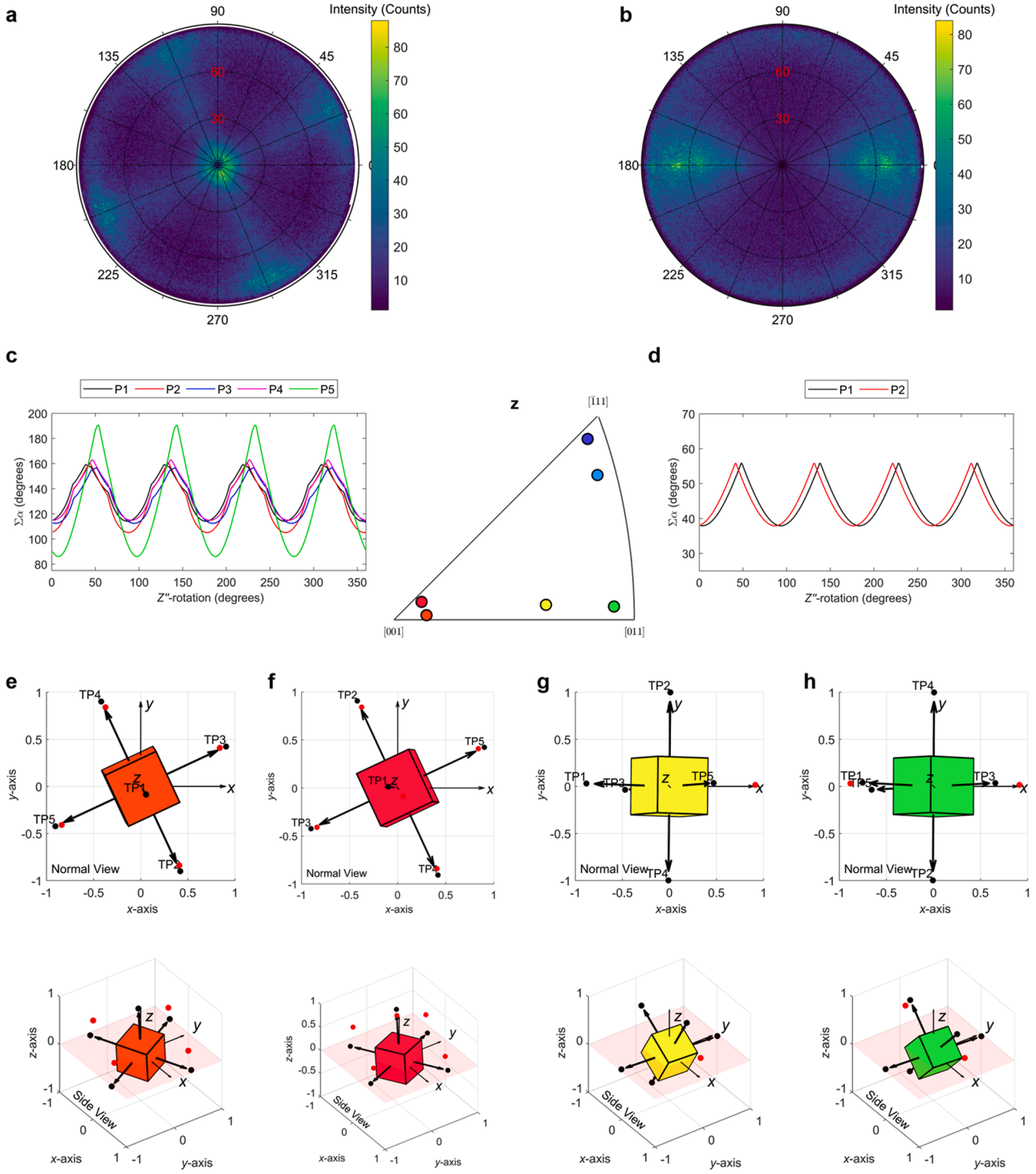

Fig. 5. Orientation extraction from etched single crystal surface topography. Topography intensity profile of a) [100] and b) [110]-oriented Al. Angular difference minimisation plots for the [100] (c) and [110] (d) oriented specimens, respectively. Center) IPF (z vector) showing the extracted orientations of all single crystal specimens colored to their position on the IPF, for both the vector matched and best fit approaches (see Fig. 4 for reference to [111]-oriented specimen). Reconstructed crystal shapes for the [100]-oriented sample: e) vector matched, f) best fit, and for the [110]-oriented sample: g) vector matched, h) best fit, colored according to their positions on the IPF (For interpretation of the references to color in this figure legend, the reader is referred to the web version of this article.).

approach where there is one high-intensity peak with a well-defined elevation. Intuitively, this is limited to ≈[100]-oriented crystals where a large fraction of the surface area is normal to the microscope (i.e. flat) and easy-to-measure. For other orientations where the peaks occur at higher elevations, vector matching will typically return a less accurate result as, for the aforementioned reasons, our confidence in the peak elevation angle reduces at higher elevation angles. This was incorporated as a selection rule that is triggered when $> 20\%$ of the total intensity of the TIP occurs at an elevation $< 20^{\circ}$ (*20 under 20*). If this criterion is not triggered, then the best fit approach is used to index the topographic peaks.

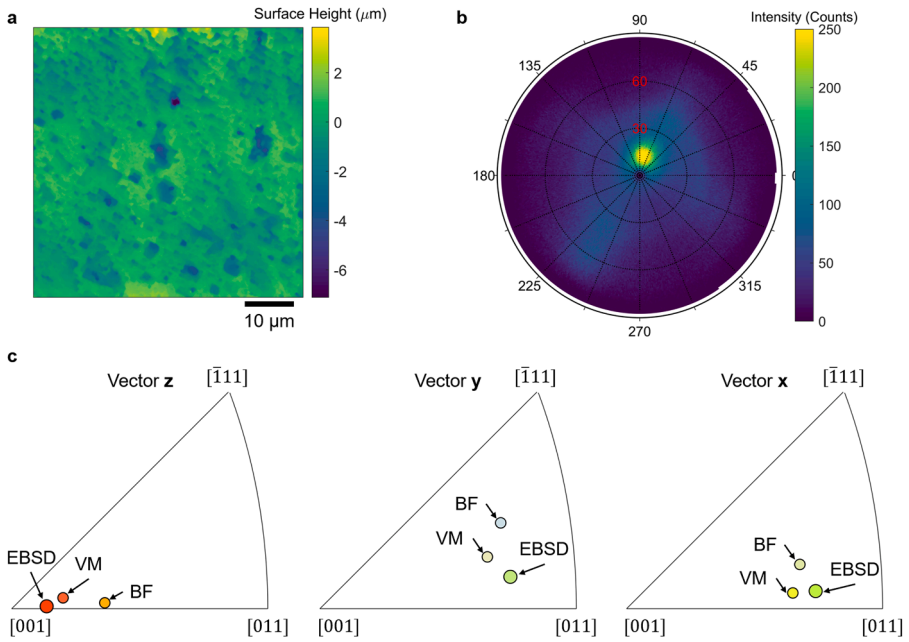

Fig. 6. Predicted topography profile and surface data comparison. a) Surface topography of an Al-6082 grain vicinal to [100]. b) The resulting TIP for this grain with the corresponding IPFs for the z, y, and x directions comparing the EBSD to both the vector matching (VM) and best fit (BF) approaches (For interpretation of the references to color in this figure legend, the reader is referred to the web version of this article.).

3.3. Orientation assessment over a planar surface

In order to demonstrate this technique, a polycrystalline sample of large grained (but a commercial grade) Al-6082 was etched using the slot jet to reveal a relatively large measurement area (≈400 mm^2), according to the parameters outlined in Section 2.2 (Fig. 7a). Surface preparation time was 95 s, consisting of two etching passes (20 mm) along the machining *y*-axis offset by 9 mm along the *x*-axis. Theoretical etching depth was calculated from Faraday's law to be 12.7 μm at these parameters in this material, which broadly corresponds with the measured depth for both passes (11.87 ± 0.85 μm, 12.99 ± 0.94 μm), shown in the mean depth profile from the unetched surface in Supplementary Fig. 3. Intuitively in the overlap region, subjected to two equivalent etching passes, etch depth is approximately double the theoretical depth, which indicates that the extent of this overlap can be reduced for further large area etching routines. This central overlap region is shown in the relative surface height map in Fig. 7b, and the surface gradient map in Fig. 7c. Both maps are sampled at the mapping resolution of the topography orientation image (TOI), to facilitate pixelwise analysis.

EBSD was performed prior to etching as the depth removed was designed to be significantly less than the average grain size (mean diameter 675 μm, mean area 264,000 μm^2), where the resulting **z, y**, and **x** projections of the IPF shown in Fig. 7d, corresponding to the red box in Fig. 7a. This dataset was considered as the ground truth against which to compare the topography orientation image (TOI), shown in Fig. 7e for the same IPF projections.

A flow diagram showing the routine used to identify characteristic peaks from the TIPs is shown in Supplementary Fig. 4. No data is returned where only one characteristic peak can be identified from the TIP. Informed by Section 3.1, sampling areas of 12,100 μm^2 (110 × 110 μm) were used for orientation mapping, where data was sampled with a sliding window (step size 55 μm) to enhance apparent mapping resolution. Here, two steps in *x* or *y* are required for a new sampling area to be completely independent of an initial sampling area.

In addition to pixelwise orientation mapping, extracting grain-resolved microstructural information is desirable as it enables the statistical analysis of different microstructural factors including grain boundary character, orientation relationships, and grain shape parameters, all of which can influence the mechanical and functional properties of materials. To appraise the suitability of TOI towards this, grain shapes were extracted from the TOI data applying a misorientation threshold of 7° and removing small grains (< 5 pixels threshold). This was achieved after applying a median filter (1 nearest neighbor, 3 × 3 grid) to the TOI data, where the resulting orientation map (IPF-z), with overlaid grain boundaries is shown in Fig. 8a (grains < 25 pixels not displayed). Full maps corresponding to the EBSD data, unfiltered, and filtered TOIs are displayed in Supplementary Fig. 6, with grain boundaries overlaid.

Apparent color jumps can be observed in some of the grains in Fig. 8a, which is reflected in the kernel average misorientation (KAM) map of the same area (Fig. 8b), showing subgrain boundaries in some cases displaying a greater KAM value than the 7° misorientation threshold applied for grain discrimination. This implies there are fluctuations in the calculated misorientation along a given grain boundary that prevent the satisfactory reconstruction of the discrete grains. This might be partially due to grain boundary artefacts, which might also act to reduce the misorientation gradient between adjacent grains and challenge their reconstruction. Fig. 8c shows the spread of grain orientations within the extracted grains, where high magnitude spreads are associated with grains having noticeable color jumps in Fig. 8a and subgrain boundaries in Fig. 8b. Nevertheless, the boundary misorientations, which can be associated with grain boundary character, can be extracted and plot (Fig. 8d), and these results can be aggregated over the entire TOI dataset (boundary misorientation distribution, Fig. 8e).

Orientation-based approaches to grain discrimination could also be augmented by correlative microscopy. Concomitant optical microscopy is possible using most off-the-shelf topography measurement solutions (including the one used in this study). Thus, it is reasonable that practical application of TOI could be augmented by simultaneous conventional optical imaging, where correlative measurements can be acquired without increasing measurement time or intervention.

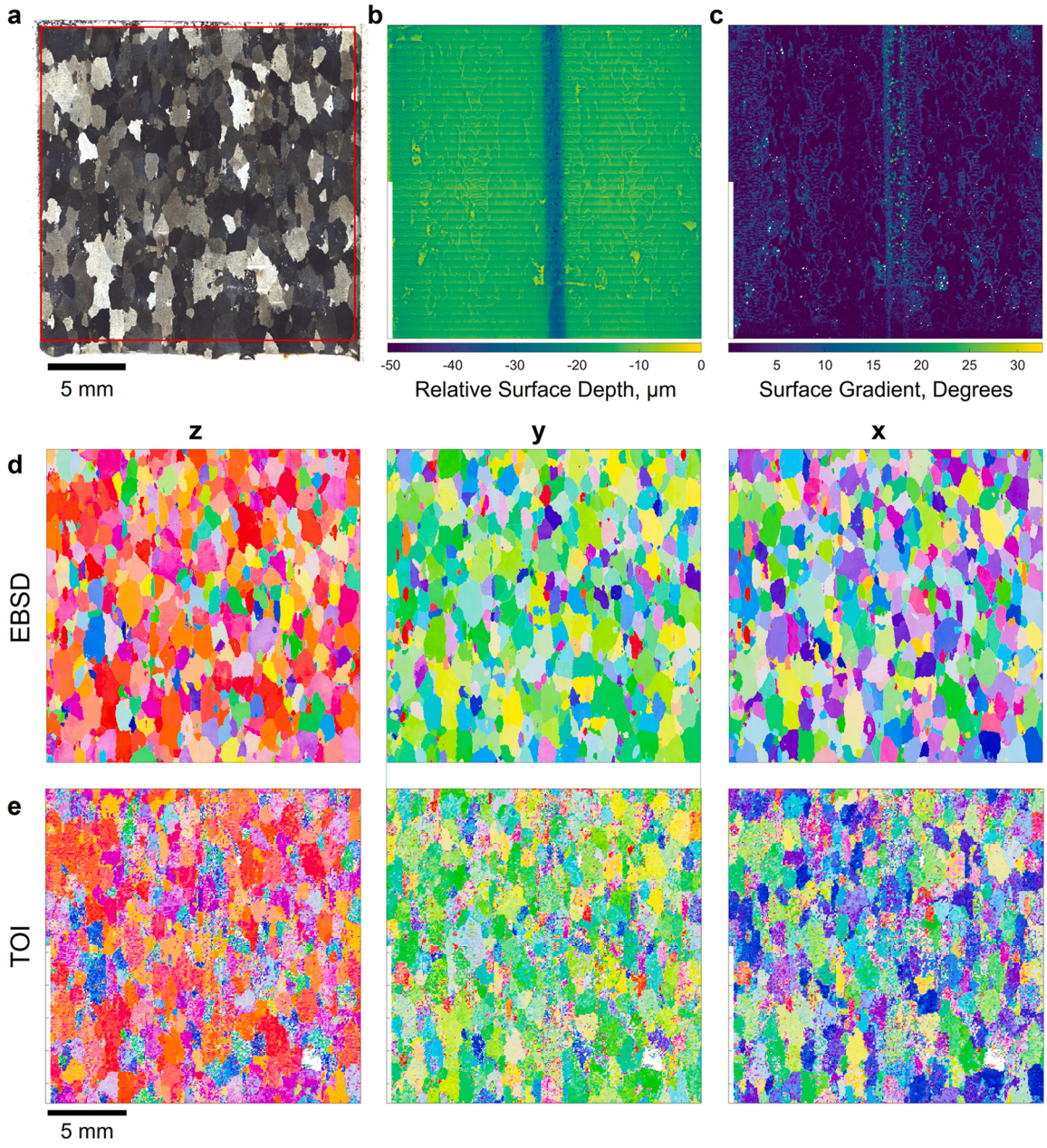

Fig. 7. Large area orientation mapping over a generated planar surface (≈400 mm^2). a) Optical micrograph of a large area (≈400 mm^2) planar etched surface of an Al-6082 polycrystal (topography data acquisition region denoted by red box). b) Average surface height for each measurement region (320 × 320 regions at 55 μm step size), showing the deeper central region where the overlap of the two parallel etching passes. c) The elevation (surface gradient) of each measurement region. d) EBSD maps (960 × 960 pixels) for the same Al-6082 polycrystal (prior to etching) colored for the z, y, and x IPF projections. e) Corresponding topographic orientation maps (320 × 320 pixels) for the same field of view colored to the same projections (data presented at 55 μm/pixel). HSV coloring used in d) and e) (For interpretation of the references to color in this figure legend, the reader is referred to the web version of this article.).

3.4. Accuracy and sources of error

The TOI allows the resolution of orientation, where the maps are comparable to the EBSD data; a caveat being that the results in the **y** and **x** projections are dependent on the relative in-plane rotation of the sample during both EBSD and topography data acquisition. In both cases, alignment in Fig. 7 was performed manually and thus there is an uncertainty, the magnitude of which is likely to be small (e.g. $< 3°$) but is ultimately undefined. This source of error was reduced by registering the two datasets together prior to misorientation comparison, described in Section 2.3).

The EBSD data (960 × 960 pixels) was binned to the same resolution as the TOI dataset (320 × 320 pixels) to allow direct pixelwise comparison. The two datasets were directly compared by calculating the misorientation between each given pixel, plot as orientation distribution functions for the **z, y**, and **x** projections (Fig. 9a), colored according to the misorientation map, which is shown alongside in Fig. 9b. There is a slight dependence of misorientation on the underlying grain orientation. Orientations vicinal to [001] tend to agree more with the EBSD data (i.e. return a smaller misorientation), while larger misorientations appear to be associated to orientations vicinal to [011]. This corresponds to the results observed in the single crystal study (Fig. 5e), which indicated the efficacy of characterization correlated to the number of characteristic peaks present in the TIP.

This can be further demonstrated by segregating the misorientation map according to the magnitude of the Euler angle Θ extracted from the

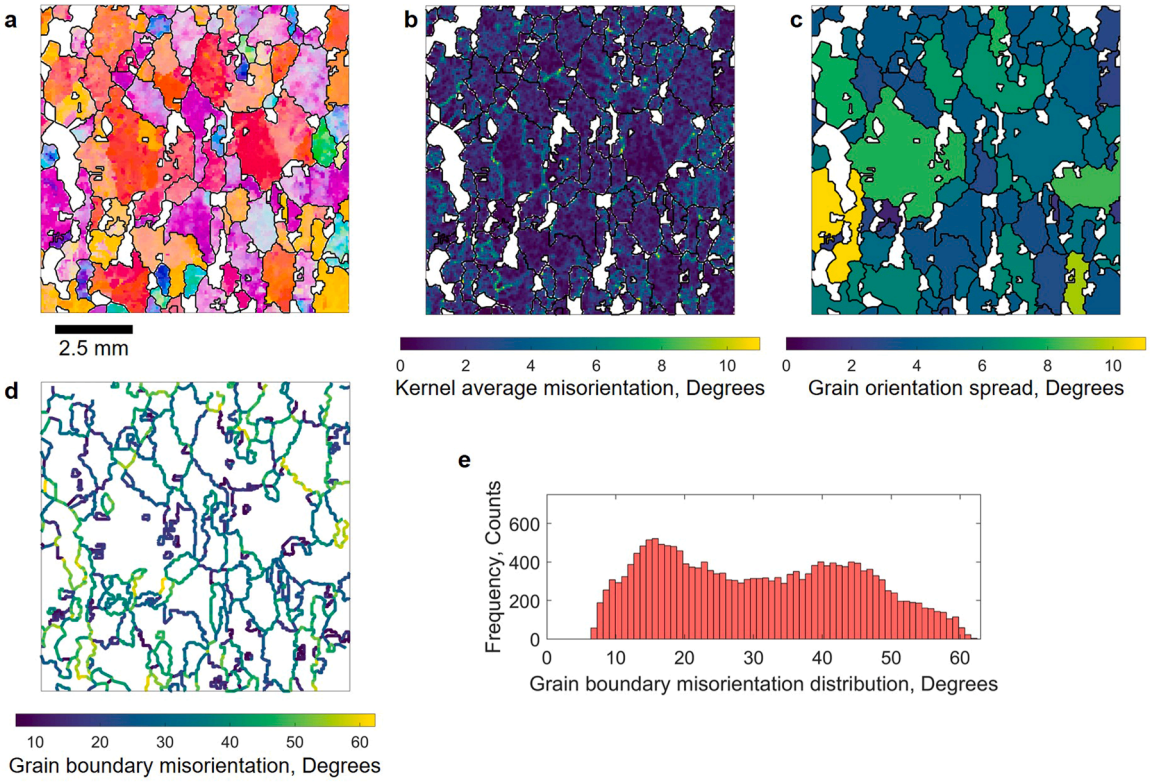

Fig. 8. Processing TOI data can allow grain reconstruction and extraction of grain properties. a) Orientation map (IPF-z), with boundaries overlaid of grains reconstructed from the TOI data using a 7° misorientation threshold (grains < 25 pixels not displayed). Orientation map constructed after applying a median filter (1 nearest neighbor, 3 × 3 grid). b) Kernel average misorientation map, c) grain orientation spread, and d) grain boundary misorientations of the same field of view as a). e) Histogram showing the aggregated grain boundary misorientations over the entire TOI dataset (For interpretation of the references to color in this figure legend, the reader is referred to the web version of this article.).

TOI, shown in Fig. 9c–d for $\Theta < 20°$ and $\Theta > 20°$, respectively. For small Θ magnitudes ($< 20°$), misorientation is lower than for larger magnitudes ($> 20°$), broadly correlating with the expected presence of a high intensity peak at low values of Θ that aids the indexing step. At higher Θ angles, the topography the model returns a best fit between extracted peaks, which can be difficult to define due to the formation of artefacts such as rays across the topography intensity profile.

The misorientation error with respect to EBSD was quantified with the aid of histograms, shown for the entire map, $\Theta \langle 20°$, and $\Theta \rangle 20°$ in Fig. 9e and f, respectively. The mean misorientation value is 32° across the map, which is marginally lower for the $\Theta < 20°$ threshold (29°) than for the $\Theta > 20°$ threshold (33°), while the 90th percentile is 49° across the entire dataset.

Areas of high misorientation appear to be localized over discrete grains in Fig. 9b–d. To investigate the origin of these errors, separate grains having high ($> 45°$) average misorientations were investigated comparing the EBSD data with the TOI output. As such, grains arbitrarily named '1′ and '2', were investigated given their high mean misorientation relative to EBSD (49° and 51°, respectively), and their boundaries are displayed on the misorientation map in Fig. 10a (EBSD red, TOI black). Grain shapes extracted from Grain 1 and Grain 2 are shown in Fig. 10b and c respectively, where i) is the error map (extracted from Fig. 10a), ii-iii) the extracted grain shapes from EBSD and TOI respectively. iv) Shows a characteristic TIP from a topography area within iii) and v) shows visualisations of the orientations returned by EBSD (red outline) and TOI (black outline). In both cases, the TOI results correlate well with the accompanying TIP, and thus the revealed etch facets at the surface (surface height maps shown in Supplementary Fig. 7).

Considering the EBSD data as the ground truth, Grains 1 and 2 share similar orientations, where both are vicinal to [011] and separated by an in-plane rotation. This correlates with the higher error associated with [011]-vicinal orientations shown in the orientation distribution in Fig. 9a. For both Grains 1 and 2, the EBSD and TOI results are separated by an in-plane rotation of approximately 90° as indicated by the accompanying visualisations. Taken together, it is possible that the facets are forming on symmetrically equivalent {001} planes, the azimuthal directions of which are orthogonal in this projection. Nevertheless, despite returning a lattice direction that is orthogonal to EBSD, even in this high-error case, TOI can adequately return the grain 'texture' in the normal direction, although the IPF coloring in the corresponding **x** and **y** projections are essentially inverted with respect to the EBSD.

Indexing quality can also become poorer in the vicinity of a grain boundary, particularly through the superimposition of TIPs when sampling topographies over a grain boundary. As this method relies on the ability to accurately extract peak positions from the TIPs, it is vulnerable to instances where a sampling region falls over a grain boundary.

This effect is shown in Fig. 11, where an area of topography over a grain boundary is sampled, with the boundary running approximately vertically in the center of the field of view (i.e. a bi-crystal region). The corresponding TOI of this region (Fig. 11b) indicates the existence of *a* ≈[110]-oriented region at the boundary between the two grains. Both grains (arbitrarily named 'i' and 'ii') return characteristic TIPs (Fig. 11d) that allow their orientations to be indexed, however as their dominant peaks are azimuthally separated by ≈180°, the superimposition of their patterns challenges the accurate indexing of the boundary region (Fig. 11e), resulting in orientations vicinal to [110] occurring as a discrete vertical band between the two grains, which is (erroneously) reflected in the corresponding TOI in Fig. 11b. This was confirmed by SE imaging of the boundary region (Fig. 11f, field of view inset Fig. 11c middle), where the exposed etch facets appear to correlate with the TOI-indexed crystal shapes for Grains i and ii, shown in Fig. 11e. This type of

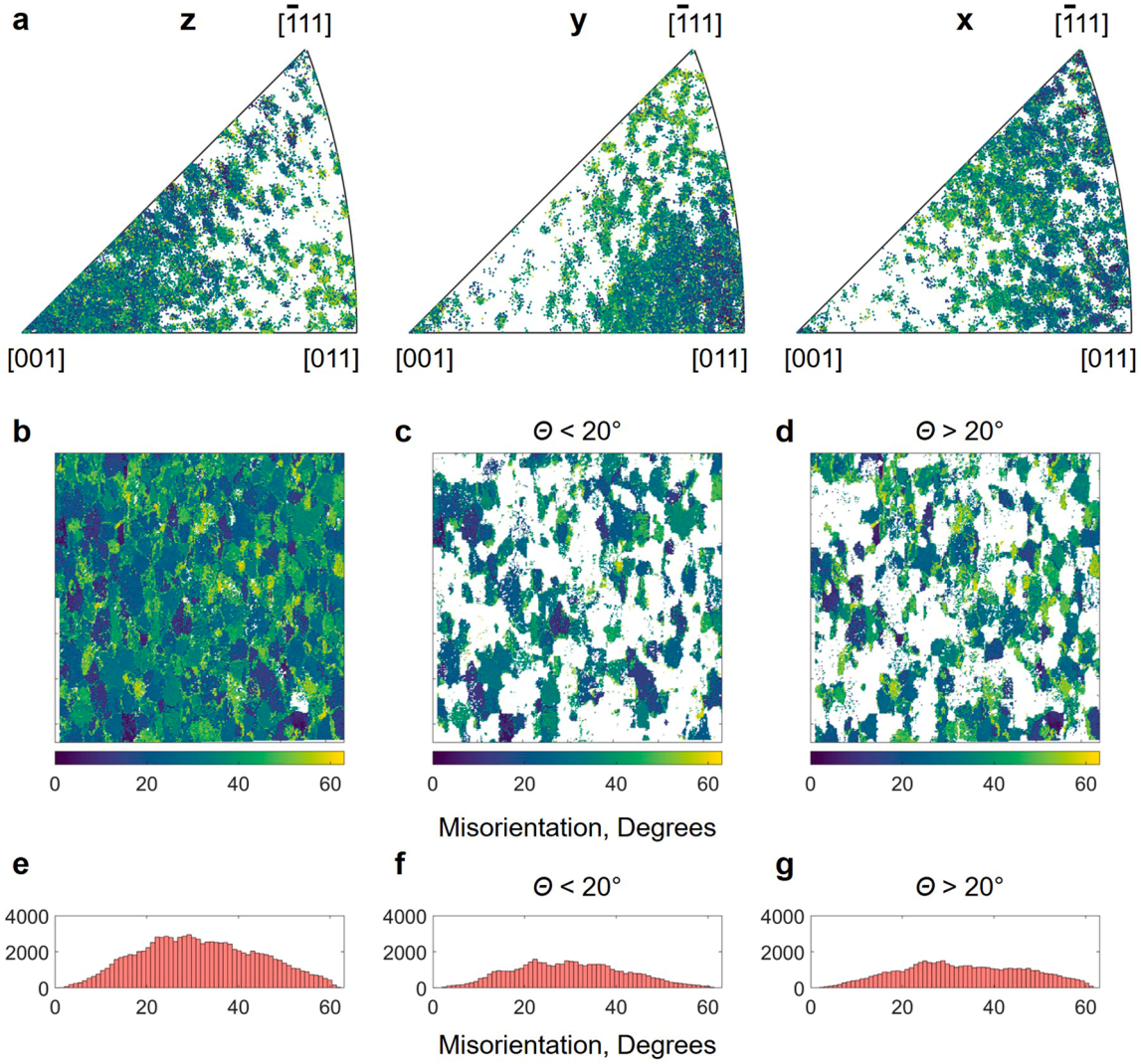

Fig. 9. Misorientation between TOI and EBSD datasets. a) EBSD orientation distribution function colored according to the misorientation with the TOI for the z, y, and x projections (see (b) for coloring). b) Misorientation map comparing EBSD to the TOI (raw unfiltered data). d) Heat map showing the difference in Euler angle Θ between EBSD and the TOI. e) EBSD orientation distribution function colored according to the misorientation with the TOI for the z, y, and x projections (see (c) for coloring) (For interpretation of the references to color in this figure legend, the reader is referred to the web version of this article.).

artefact could be reduced by adapting the data processing method [45], for instance comparing the TIPs with a dictionary of simulated patterns (including bicrystal patterns), or by giving a weighting to certain peaks based on their relative intensity (Supplementary Fig. 8), in addition to retrospectively considering peaks extracted from neighbouring fields of view.

3.5. *Orientation mapping over complex features*

A key advantage of topographic measurement is that the data acquisition is, by design, robust to changes in surface geometry over a given analysis region. Given that etch facet micro-topographies are dictated by the underlying crystalline orientation, they are broadly independent of the longer wavelength macroscale surface topography. Accordingly, orientation extraction should be robust to changes in surface geometry. This implies that a flat measurement surface is not required; any arbitrary surface geometry can be analyzed and orientation information can be extracted, so long as i) topography data can be acquired from the surface, noting the line-of-sight nature of optical metrology, leading to a sensitivity towards high surface gradients, and ii) the macro-topography wavelengths associated with the surface geometry can be adequately separated from the etch facets.

To test this hypothesis, we exploited the capability of the electrolyte jet machine tool to mill out a complex geometry pocket in a polycrystal sample (setup shown in Fig. 12a). This was achieved by varying the feed rate of the nozzle during etching to vary the effective areal charge density that dictates the etch depth, rather than changing the surface current density, which can alter the length scales of the etch facets [25]. Fig. 12b shows a reconstruction of the resulting surface with superimposed with areal charge density values. Fig. 12c shows a reconstruction of a typical section of an etched measurement area, which has an associated longer wavelength form, indicated by the extracted least squares plane (Fig. 12d). The surface normal of this plane is used to define the elevation (i.e. the surface gradient) of a given measurement region. Fig. 12e shows an optical micrograph of the region of interest of the etched surface indicated by the dashed box in Fig. 12b, and the corresponding TOI is shown for this region in Fig. 12f. This allows the observation of grain orientations despite the differing surface height (Fig. 12g) and elevation (Fig. 12h) of each measurement area.

The ability to measure orientation over non-planar surfaces poses an interesting challenge, namely that more than one orientation can be considered: i) the orientation of the crystal relative to the microscope reference axis, and ii) the orientation of the crystal relative to the normal of the measured surface. In this study, we have presented the former

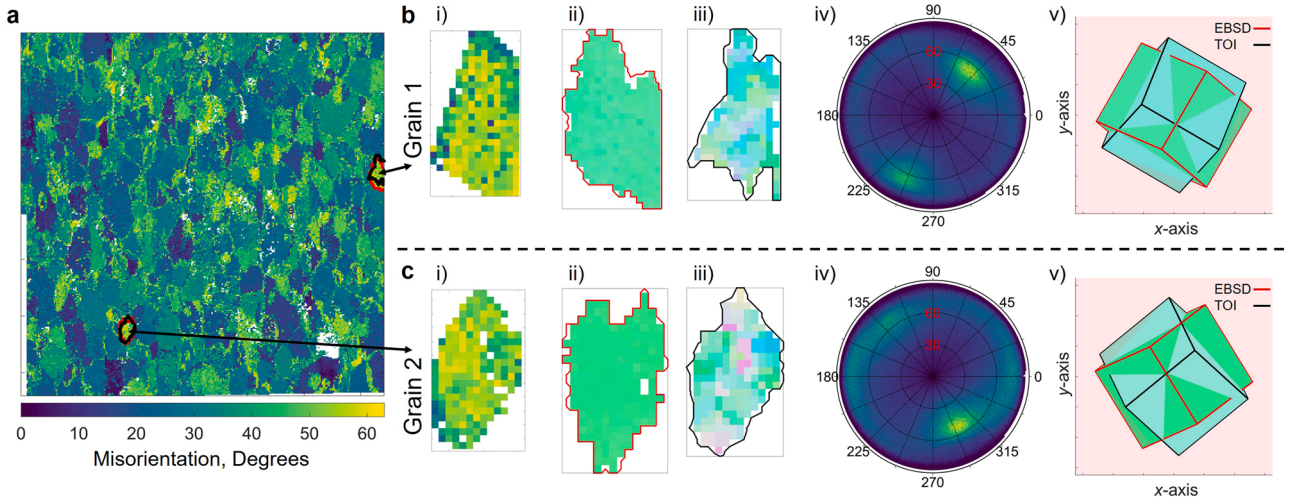

Fig. 10. Comparative study of high error (> 45°) grains. a) Misorientation map with two high error grains outlined (EBSD red, TOI black). Grain 1 b) (49° error) and Grain 2 c) (51° error): i) Error map extracted from a) as the convex hull of the TOI grain shape. ii) EBSD (red outline) and iii) TOI (black outline) grain shapes, respectively. iv) TIP calculated from a representative area of topography in iii). v) visualization (z projection) of the resulting crystal shapes calculated from EBSD and TOI (red and black outlines, respectively), colored according to the mean orientation (For interpretation of the references to color in this figure legend, the reader is referred to the web version of this article.).

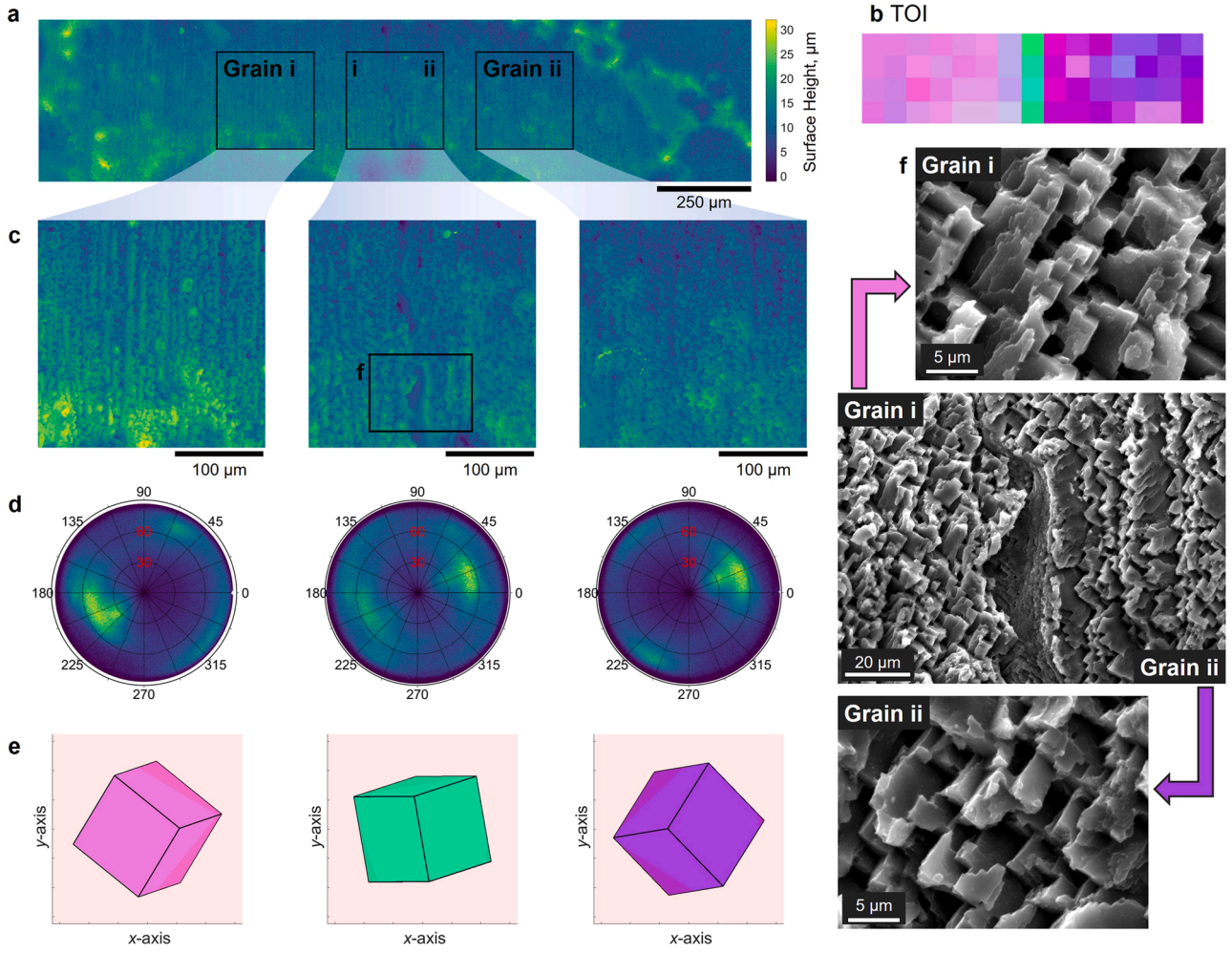

Fig. 11. Superimposition of grains can complicate grain indexing from TIPs. a) Topography field of view showing Grains 'i' and 'ii', with three sampling areas of interest (AOIs). b) TOI of the approximate area shown in a). c) Topographies of the AOIs shown in a) and d) the corresponding TIPs for these AOIs. The middle TIP is the superimposition of the Grains i and ii. e) crystal shapes corresponding to the orientations extracted from the TIPs. f) Secondary electron micrographs of Grain i (top), the boundary area (middle, also inset in the topography AOI in c), and Grain ii (bottom) (For interpretation of the references to color in this figure legend, the reader is referred to the web version of this article.).

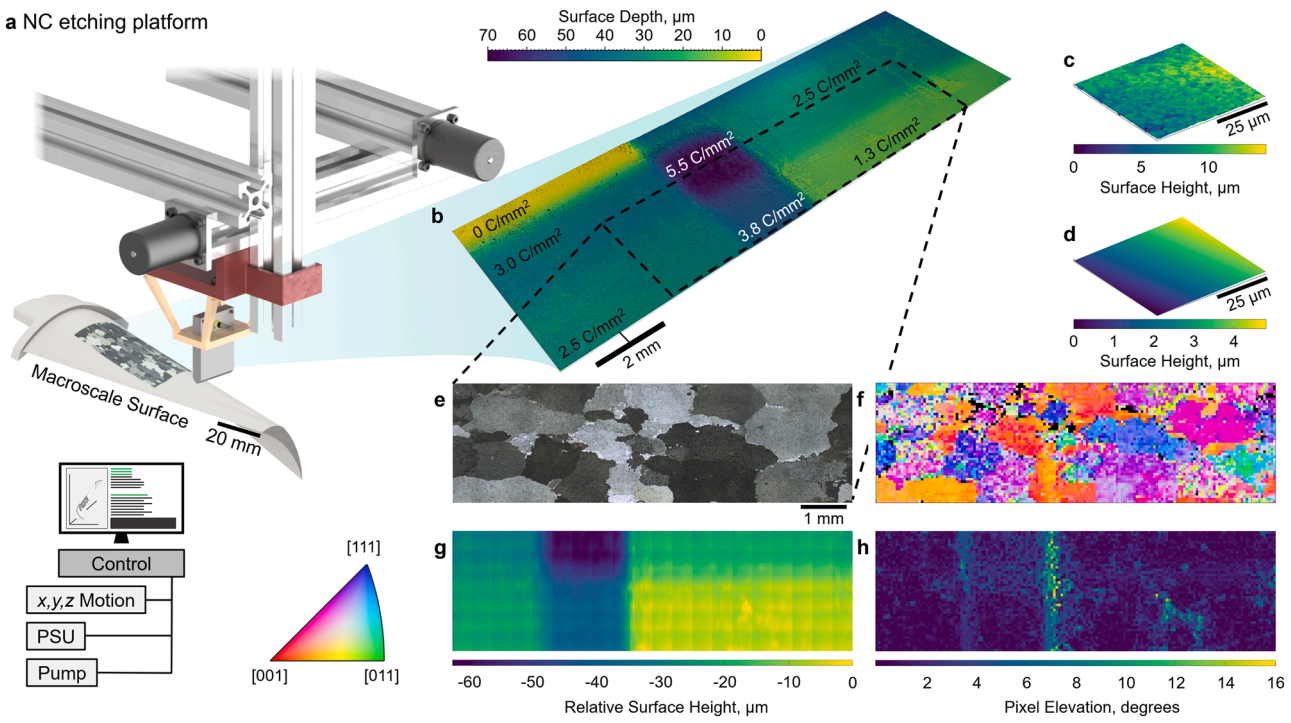

Fig. 12. Orientation measurement over different surface depths. a) A vision for a numerically controlled etch platform with integrated metrological capability. b) Reconstruction of the surface created using the electrochemical jet machine tool to create measurement areas at different surface depths, corresponding to areal charge density. Measurement area denoted by dashed box. c) A surface area (3000 µm^2) showing etch facets and d) the least squares plane of c). The surface gradient of the field of view is taken as the normal vector of this plane. e) Optical micrograph of etched global measurement area. f) Topography orientation image (z-projection) of the global measurement area in e) alongside the relative height (g) and elevation (h) of each measurement area (For interpretation of the references to color in this figure legend, the reader is referred to the web version of this article.).

(Fig. 12f). However, this may not always be the best approach. As an extreme example, consider orientation measurement of etched grains around the entire outer circumference of a pipe section; in this case the orientation with respect to the surface normal will likely yield more valuable information.

It is anticipated that methods incorporating TOI routines could find use as part of a low-intervention materials characterization approach or diagnostic tool on the factory floor that can be implemented independently of sample size. To demonstrate this opportunity, a sample of Al-alloy was processed with single laser tracks to melt the surface according to the parameters listed in Section 2.1 to simulate a weld.

This was selected as a commonly used manufacturing process that has an obvious and significant effect on the local microstructure, surface geometry, and surface chemistry. As such, it presents a challenging materials characterization subject. Parts that are laser welded or laser heat treated typically require quality control or further assessment, depending on the nature and target application of the part. While there are different non-destructive methods to characterize the density of welds and the presence of defects including cracks and pores [46], appraising the microstructure remains a challenge without postmortem examination (e.g. after sectioning). In addition to altering the microstructure, welding processes also typically change the local surface height through the generation of a weld bead, particularly where a filler material is used. They may also change the surface chemistry (e.g. through oxidation), especially in cases where it is difficult to control the degree of shielding. Taken together, these factors present a characterization challenge to which TOI has been applied, in this case to observe orientation relationships between adjacent grains outside of and within the laser-processed fusion zone, without sectioning the sample.

Fig. 13a shows an optical micrograph of an Al-alloy sample that has been processed with three single laser scan tracks (20, 60, and 100 mm/s, scanned left to right) and subsequently etched using the setup. These laser parameters are expected to form columnar grains [47]. The resulting TOI orientation maps are shown in Fig. 13b for the **z** and **y** directions. A clear textural difference can be identified within the fusion zones of all the laser scan tracks. The mean heights of each pixel are shown in Fig. 13c, across a total height range of 0.13 mm. In addition, the mean elevation (surface gradient) of each pixel is shown in Fig. 13d. High magnitude surface gradients (up to 58°) associated with the weld beads are apparent, representing a challenging surface for materials characterization.

A small subsection of this data was the subject of further study. The area of interest, which spans a fusion boundary corresponding to the 100 mm/s track, is marked by the red box in Fig. 13a. The topography associated with this area of interest is shown below center, with four marked regions (200 × 200 µm) corresponding to four discrete grains (arbitrarily named *i-iv*). Grains *i* and *iii* fall outside of the fusion zone and grains *ii* and *iv* fall within the fusion zone. Here, grain *i* is adjacent to grain *ii* and grain *iii* is adjacent to grain *iv*. The limit of the fusion zone can be determined by the discrete approximately horizontal line spanning the width of the area of interest (marked with arrows). The topography, corresponding TIP, and the resulting crystal shape associated with the output orientation are shown in Fig. 13e–h for grains *i-iv* respectively (colored according to the IPF key).

While grain *i* is adjacent to grain *ii*, the relative misorientation, $\Delta \boldsymbol{G}$, between the two grains is high (42°) and it might be concluded that grain *i* is unlikely to be the 'seed' grain in this case. If it is assumed that crystal growth during solidification occurs along the ⟨100⟩ directions in fcc materials [48,49], it could explain the high misorientation as there is no apparent [100] direction parallel (or close to parallel) to the expected grain growth direction that would be anticipated from the laser scan path. The relationship between grains *iii* and *iv* is much closer, with a relative misorientation of 13° This might be intuitive, given a [100] direction appears to align more closely with the expected direction of grain growth. On balance, this could indicate that grain *iv* has been seeded from grain *iii*.

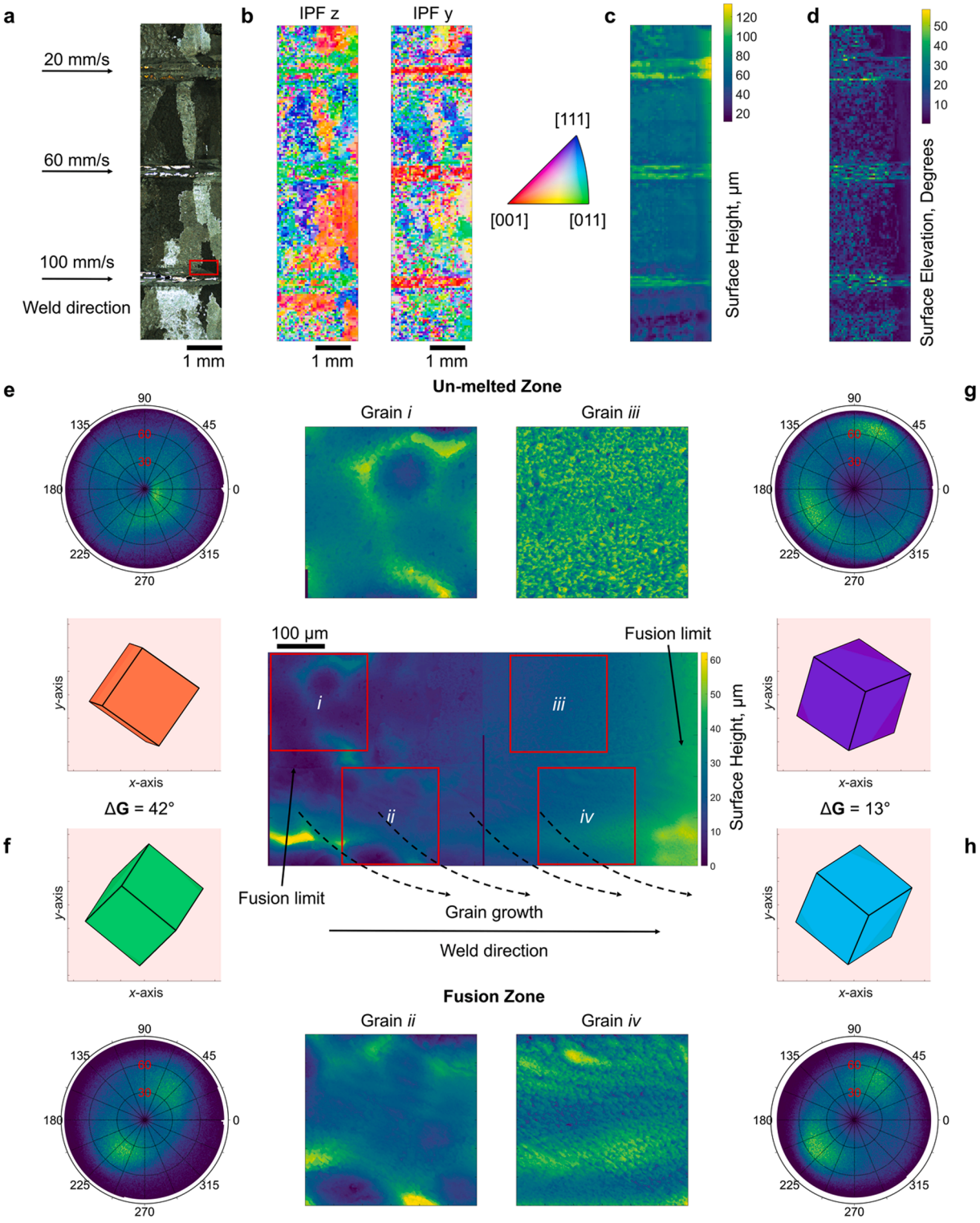

Fig. 13. Orientation measurement over weld track artefacts. a) Optical micrograph of a laser processed Al-alloy sample (red box outlines area of interest for study in e-h). b) TOIs for the z and y directions for this field of view with accompanying color key. c) Surface height map calculated from the mean height of each pixel in b). d) Surface gradient map calculated from the mean elevation of each pixel in b). e-h) Region of interest, TIP, and resulting crystal shapes corresponding to grains i-iv. Center) area of interest shown in a) with regions corresponding to grains i-iv) outlined in red (For interpretation of the references to color in this figure legend, the reader is referred to the web version of this article.).

3.6. *Extracting orientations from different alloys*

Characteristic faceting behavior is not fixed for a given crystal system. For example, while the slow etch directions, thus the topography, of Al follow ⟨100⟩, other fcc materials like Ni facet along the ⟨111⟩ directions when exposed to identical electrochemical jet etching treatments [25,33]. The resulting exposed (111) planes are offset from the unit cell orientation by a z-rotation of 45° To validate the applicability of

the methodology towards different faceting behavior, the approach was adapted to study a sample region of commercially pure Ni. In this case, a region of this material was etched and measured using CSI, detailed in Section 2.1. The surface topography dataset of the measurement area is shown in Fig. 14a, alongside the **z** projection of the resulting EBSD data corresponding to approximately the same area (Fig. 14b), and the resulting topography orientation image (**z** projection) extracted from the surface height map (Fig. 14c).

The TOI was generated with a 98 × 98 μm sampling region and oversampled with a 24.5 μm step size. To generate the TOI in Fig. 14c, TIPs were constructed in an identical manner to Al, but were matched against a vector set corresponding to the face normals of the (111) crystallographic planes. The final Φ_2 Euler angle was composed of the matched Φ_2 angle and an additional rotation of 45° to account for the difference between the (111) planes and the unit cell.

A comparison was performed between the topography method and EBSD for three different sampling areas, corresponding to the red boxes in Fig. 14a and the black boxes in the EBSD data (mean orientation, Fig. 14b). Topography sampling areas are shown in Fig. 14d-f (column i), with the resulting TIPs for each sampling area (column ii), and orientation visualisations (including the constructed (111) planes) extracted from the topography method (column iii). The equivalent crystal shape orientation visualisations from the EBSD data (calculated as the mean orientation within each black box area in Fig. 14b) are given in column iv, where both sets of visualisations are colored according to the IPF. The misorientation between the two datasets, $\Delta \boldsymbol{G}$, is shown between, ranging from 11° - 30°

Interestingly, orientations closer to [100] and [110] (Fig. 14e and f) return lower misorientation with EBSD than the grain closer to [111] (Fig. 14d); this is similar to Al, despite the fact that low angle etch facets are flatter and typically easier to measure by metrological methods. This can also be observed by comparing the maps in Fig. 14b and c. This can be partially explained by observing the TIP in Fig. 14dii, which indicates that the surface is dominated by large area facets of a single orientation that leads to a very high intensity low angle peak. This obfuscates the identification of secondary peaks and therefore challenges the indexing

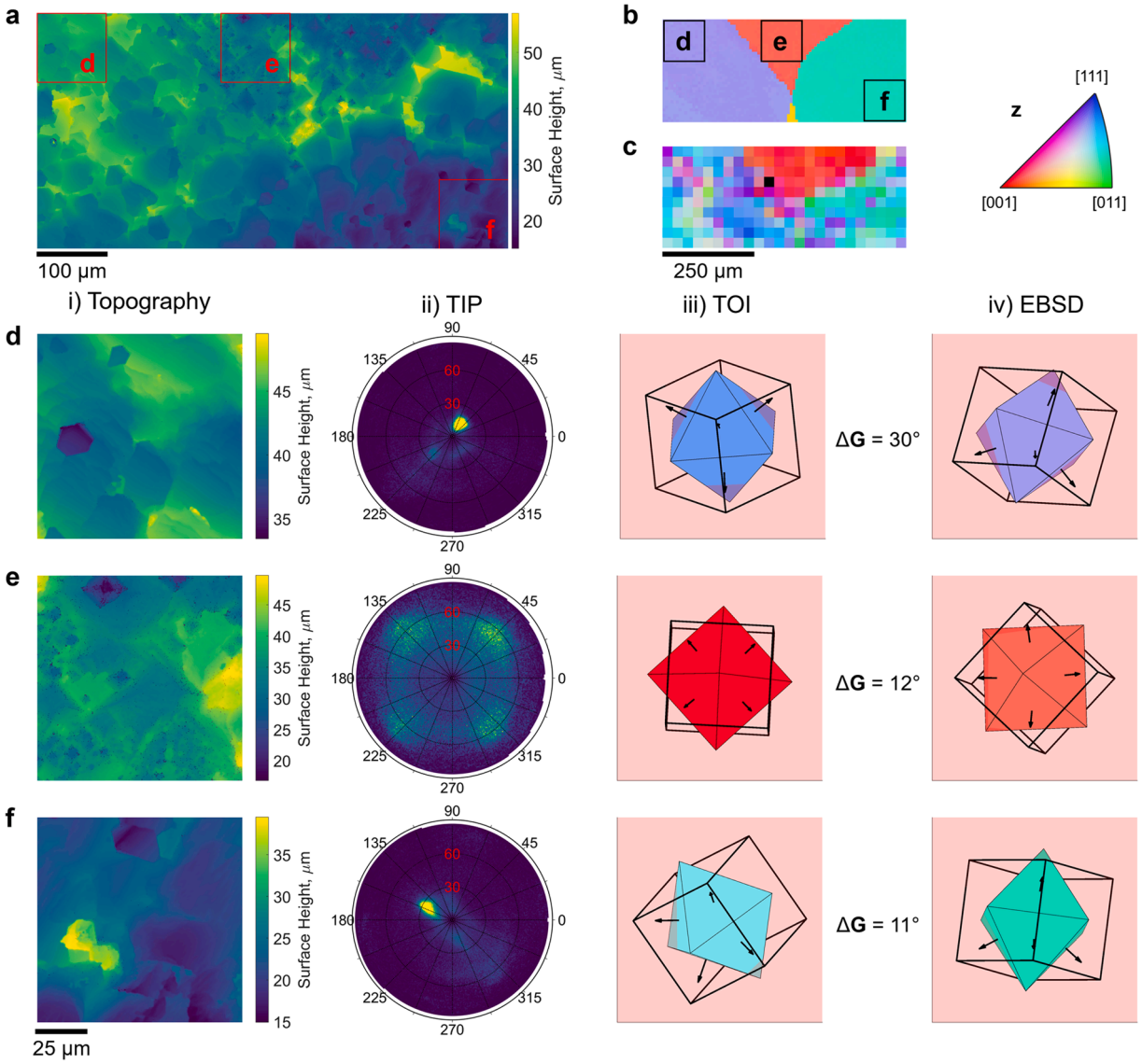

Fig. 14. Orientation measurements in Ni. a) Surface height map (CSI data) of the measurement area (red boxes indicate areas of interest). b) EBSD map (IPF-z) of the approximate area in a), with c) the accompanying TOI extracted from the surface height map. d-f) Column i) different topography areas of interest outlined in a), ii) the corresponding TIP extracted from each area of interest, iii) a crystal shape visualization of the extracted orientation through the TOI method, and iv) crystal shape visualization of the EBSD extracted orientation (For interpretation of the references to color in this figure legend, the reader is referred to the web version of this article.).

process. This effect might be reduced by modifying the etching parameters for this material in order to generate finer facets with more secondary directions.

4. Conclusions and future perspectives

To conclude, we have coupled a numerically controlled production line compatible electrochemical machine tool with automated surface topography measurement to selectively etch materials of high symmetry ($\geq$ order 24) and characterize the resulting topographic etch response under ambient conditions. From these large area topographies (up to 400 mm^2), we have acquired orientation information pertaining to the underlying crystalline grains. We have demonstrated that standard grain segregation routines can be applied to the collected datasets to yield microstructural data like grain shape parameters, local texture, and grain boundary misorientation distributions. These are understood to affect the functional and mechanical properties of materials and are therefore will be valuable for manufacturers if such data can be collected on the factory floor. In addition, we have indicated that our measurement approach is robust to differences in surface height and differences in surface gradient (up to 58° tested on the simulated weld tracks in this study). This opens a new route through to non-destructively assessing grain orientation over complex surfaces, without needing a flat measurement surface, noting that high-value parts typically have complex geometries by design.

We have characterized the spatial resolution limits and orientation accuracy using our approach against EBSD; these are defined by our ability to create and measure etch facets over a surface. The accuracy of our method is sensitive to the determination of peak positions, corresponding to aggregations of similarly oriented etch facets, in the extracted intensity data. Due to the line-of-sight nature of optical topography analysis, our ability to accurately measure these peak positions reduces at higher facet slope angles. This is reflected in the misorientation between our results and EBSD, which is smaller where there are dominant peaks at low elevation angles, for example in Al grains vicinal to [100]. The mean misorientation error between TOI and EBSD was 31° over a large area dataset (400 mm^2). Instances of high error were investigated indicated to be caused by certain grain boundaries and in some cases are understood to result from preferential etching along symmetrically equivalent planes.

The TOI method is currently limited to materials with grain sizes of approximately 100 μm and above, more sophisticated data processing routines might be able to deconvolute different sets of characteristic peaks from the same TIP, where two differently oriented grains are sampled in the same sampling area. For example, grains finer than the spatial resolution limit could be resolved by sub-diving each topography field of view and then comparing the TIPs acquired from each subdivision to one another (Supplementary Fig. 8). By indexing the coordinates of the highest intensity peaks from within each subdivision, it should be possible to resolve grain boundaries beyond the spatial resolution required for crystallographic orientation indexing (where > 1 peaks are required). This could be compared to adjacent topographic areas to concatenate regions of high similarity, thus generating the necessary surface areas to allow orientation indexing.

Further improvements could be made by altering the TIP, for example applying correction factors to distort the data at high elevation angles, similar to fisheye correction in image processing. Alternative approaches, for example dictionary-based indexing [50] have been applied to both EBSD and DRM data [51] to improve indexing results. Given the similarities between the DRM directional reflectance profiles and the TIPs presented here, it is likely that the adoption of similar approaches will enhance topographic orientation imaging. The selectivity of the etching process itself could also be adapted to reveal alternative crystallographic planes by adding various ‘capping’ agents [52,53]. This would provide a more robust result as it would allow sequential resampling of the same material and would allow the correlation of different etch facets of the same crystal. This should make TOI more robust to instances where high elevation angle facets are generated, and also reduce high magnitude errors resulting from matching with symmetrically equivalent planes, shown in Fig. 10.

Declaration of Competing Interest

The authors declare that they have no known competing financial interests or personal relationships that could have appeared to influence the work reported in this paper.

Acknowledgments

This work was funded by the Engineering and Physical Sciences Research Council (EPSRC) under grant numbers [EP/W018942/1] and [EP/P006930/1], Eradicating hydrofluoric acid from UK metal etching, and The Future Metrology Hub, respectively. The authors acknowledge use of facilities within the Loughborough Materials characterization center and for access to the Helios PFIB, funded by the EPSRC grant EP/P030599/1, and acknowledge the facilities of the Manufacturing Metrology Team (University of Nottingham). A.T.C. would like to acknowledge the kind support of the Royal Academy of Engineering, RCSRF1920927.

Supplementary materials

Supplementary material associated with this article can be found, in the online version, at doi:10.1016/j.actamat.2023.119604.

References

[1] K. Sato, T. Yoshioka, T. Ando, M. Shikida, T. Kawabata, Tensile testing of silicon film having different crystallographic orientations carried out on a silicon chip, Sens. Actuat. A Phys. 70 (1998) 148–152, https://doi.org/10.1016/S0924-4247(98)00125-3.
[2] T. Ikehara, T. Tsuchiya, Crystal orientation-dependent fatigue characteristics in micrometer-sized single-crystal silicon, Microsyst. Nanoeng. 2 (2016) 16027, https://doi.org/10.1038/micronano.2016.27.
[3] S. Nagarjuna, K. Balasubramanian, D... Sarma, Effect of prior cold work on mechanical properties, electrical conductivity and microstructure of aged Cu-Ti alloys, J. Mater. Sci. 34 (1999), https://doi.org/10.1023/A:1004603906359.
[4] S. Uchida, T. Kimura, T. Nakamoto, T. Ozaki, T. Miki, M. Takemura, Y. Oka, R. Tsubota, Microstructures and electrical and mechanical properties of Cu-Cr alloys fabricated by selective laser melting, Mater. Des. 175 (2019), 107815, https://doi.org/10.1016/j.matdes.2019.107815.
[5] D.C. Jiles, Magnetic properties and microstructure of AISI 1000 series carbon steels, J. Phys. D. Appl. Phys. 21 (1988) 1186–1195, https://doi.org/10.1088/0022-3727/21/7/022.
[6] A. Vornberger, J. Pötschke, T. Gestrich, M. Herrmann, A. Michaelis, Influence of microstructure on hardness and thermal conductivity of hardmetals, Int. J. Refract. Met. Hard Mater. 88 (2020), 105170, https://doi.org/10.1016/j.ijrmhm.2019.105170.
[7] T.M. Pollock, Alloy design for aircraft engines, Nat. Mater. 15 (2016) 809–815, https://doi.org/10.1038/nmat4709.
[8] R. Acharya, J.A. Sharon, A. Staroselsky, Prediction of microstructure in laser powder bed fusion process, Acta Mater. 124 (2017) 360–371, https://doi.org/10.1016/j.actamat.2016.11.018.
[9] R. Shi, S.A. Khairallah, T.T. Roehling, T.W. Heo, J.T. McKeown, M.J. Matthews, Microstructural control in metal laser powder bed fusion additive manufacturing using laser beam shaping strategy, Acta Mater. 184 (2020) 284–305, https://doi.org/10.1016/j.actamat.2019.11.053.
[10] Humphreys, Quantitative metallography by electron backscattered diffraction, J. Microsc. 195 (1999) 170–185, https://doi.org/10.1046/j.1365-2818.1999.00578.x.
[11] V. Randle, Electron backscatter diffraction: strategies for reliable data acquisition and processing, Mater. Charact. 60 (2009) 913–922, https://doi.org/10.1016/j.matchar.2009.05.011.
[12] T.B. Britton, J. Jiang, Y. Guo, A. Vilalta-Clemente, D. Wallis, L.N. Hansen, A. Winkelmann, A.J. Wilkinson, Tutorial: crystal orientations and EBSD — Or which way is up? Mater. Charact. 117 (2016) 113–126, https://doi.org/10.1016/j.matchar.2016.04.008.
[13] W. Ludwig, P. Reischig, A. King, M. Herbig, E.M. Lauridsen, G. Johnson, T. J. Marrow, J.Y. Buffière, Three-dimensional grain mapping by x-ray diffraction contrast tomography and the use of Friedel pairs in diffraction data analysis, Rev. Sci. Instrum. (2009) 80, https://doi.org/10.1063/1.3100200.

[14] A.J. Shahani, X. Xiao, E.M. Lauridsen, P.W. Voorhees, Characterization of metals in four dimensions, Mater. Res. Lett. 8 (2020) 462–476, https://doi.org/10.1080/21663831.2020.1809544.
[15] F. Bachmann, H. Bale, N. Gueninchault, C. Holzner, E.M. Lauridsen, 3D grain reconstruction from laboratory diffraction contrast tomography, J. Appl. Crystallogr. 52 (2019) 643–651, https://doi.org/10.1107/S1600576719005442.
[16] N. Lu, S. Moniri, M.R. Wiltse, J. Spielman, N. Senabulya, A.J. Shahani, Dynamics of Ga penetration in textured Al polycrystal revealed through multimodal three-dimensional analysis, Acta Mater. 217 (2021), 117145, https://doi.org/10.1016/j.actamat.2021.117145.
[17] R. Patel, W. Li, R.J. Smith, S.D. Sharples, M. Clark, Orientation imaging of macro-sized polysilicon grains on wafers using spatially resolved acoustic spectroscopy, Scr. Mater. 140 (2017) 67–70, https://doi.org/10.1016/j.scriptamat.2017.07.003.
[18] P. Dryburgh, R.J. Smith, P. Marrow, S.J. Lainé, S.D. Sharples, M. Clark, W. Li, Determining the crystallographic orientation of hexagonal crystal structure materials with surface acoustic wave velocity measurements, Ultrasonics 108 (2020), 106171, https://doi.org/10.1016/j.ultras.2020.106171.
[19] O. Ilchenko, Y. Pilgun, A. Kutsyk, F. Bachmann, R. Slipets, M. Todeschini, P. O. Okeyo, H.F. Poulsen, A. Boisen, Fast and quantitative 2D and 3D orientation mapping using Raman microscopy, Nat. Commun. 10 (2019) 5555, https://doi.org/10.1038/s41467-019-13504-8.
[20] K.A. Bezjian, H.I. Smith, J.M. Carter, M.W. Geis, An etch pit technique for analyzing crystallographic orientation in Si films, J. Electrochem. Soc. 129 (1982) 1848–1850, https://doi.org/10.1149/1.2124307.
[21] M. Schneider, S. Schroth, S. Richter, S. Höhn, N. Schubert, A. Michaelis, In-situ investigation of the interplay between microstructure and anodic copper dissolution under near-ECM conditions – Part 1: the active state, Electrochim. Acta. 56 (2011) 7628–7636, https://doi.org/10.1016/j.electacta.2011.06.075.
[22] M. Seita, M.M. Nimerfroh, M.J. Demkowicz, Acquisition of partial grain orientation information using optical microscopy, Acta Mater. 123 (2017) 70–81, https://doi.org/10.1016/j.actamat.2016.10.021.
[23] X. Wang, S. Gao, E. Jain, B. Gaskey, M. Seita, Measuring crystal orientation from etched surfaces via directional reflectance microscopy, J. Mater. Sci. 55 (2020) 11669–11678, https://doi.org/10.1007/s10853-020-04734-z.
[24] D. Lausch, M. Gläser, C. Hagendorf, Determination of crystal grain orientations by optical microscopy at textured surfaces, J. Appl. Phys. 114 (2013), 194509, https://doi.org/10.1063/1.4832782.
[25] A. Speidel, R. Su, J. Mitchell-Smith, P. Dryburgh, I. Bisterov, D. Pieris, W. Li, R. Patel, M. Clark, A.T. Clare, Crystallographic texture can be rapidly determined by electrochemical surface analytics, Acta Mater. 159 (2018) 89–101, https://doi.org/10.1016/j.actamat.2018.07.059.
[26] K.-W. Jin, M. De Graef, c-Axis orientation determination of α-titanium using computational polarized light microscopy, Mater. Charact. 167 (2020), 110503, https://doi.org/10.1016/j.matchar.2020.110503.
[27] X. Wang, S. Yang, M. Seita, Combining polarized light microscopy with machine learning to map crystallographic textures on cubic metals, Mater. Charact. 190 (2022), 112082, https://doi.org/10.1016/j.matchar.2022.112082.
[28] D. Nečas, M. Valtr, P. Klapetek, How levelling and scan line corrections ruin roughness measurement and how to prevent it, Sci. Rep. 10 (2020) 15294, https://doi.org/10.1038/s41598-020-72171-8.
[29] R. Leach, C. Evans, L. He, A. Davies, A. Duparré, A. Henning, C.W. Jones, D. O'Connor, Open questions in surface topography measurement: a roadmap, Surf. Topogr. Metrol. Prop. 3 (2015), 013001, https://doi.org/10.1088/2051-672X/3/1/013001.
[30] F. Tao, J. Cheng, Q. Qi, M. Zhang, H. Zhang, F. Sui, Digital twin-driven product design, manufacturing and service with big data, Int. J. Adv. Manuf. Technol. 94 (2018) 3563–3576, https://doi.org/10.1007/s00170-017-0233-1.
[31] A. Speidel, I. Bisterov, K.K. Saxena, M. Zubayr, D. Reynaerts, W. Natsu, A.T. Clare, Electrochemical jet manufacturing technology: from fundamentals to application, Int. J. Mach. Tools Manuf. 180 (2022), 103931, https://doi.org/10.1016/j.ijmachtools.2022.103931.
[32] I. Bisterov, J. Mitchell-Smith, A. Speidel, A. Clare, Specific and programmable surface structuring by electrochemical jet processing, Procedia CIRP 68 (2018) 460–465, https://doi.org/10.1016/j.procir.2017.12.128.
[33] A. Speidel, D. Xu, I. Bisterov, J. Mitchell-Smith, A.T. Clare, Unveiling surfaces for advanced materials characterisation with large-area electrochemical jet machining, Mater. Des. 202 (2021), 109539, https://doi.org/10.1016/j.matdes.2021.109539.
[34] J. Lu, W. Liu, Y. Zhao, Anisotropy in electrochemical jet texturing of rolled stainless steel SUS304, Mater. Des. 215 (2022), 110500, https://doi.org/10.1016/j.matdes.2022.110500.
[35] J. Lu, W. Liu, X. Hu, S. Wang, G. Tang, Y. Zhao, Rapid surface preparation for three-dimensional characterization of defect and microstructure of metal additive manufacturing using electrochemical jet, Mater. Des. 212 (2021), 110180, https://doi.org/10.1016/j.matdes.2021.110180.
[36] J.H. Seo, J.-H. Ryu, D.N. Lee, Formation of crystallographic etch pits during AC etching of aluminum, J. Electrochem. Soc. 150 (2003) B433, https://doi.org/10.1149/1.1596952.
[37] J. Zhang, C. Zhao, N. Qu, Z. Shen, Improving surface quality through macro electrochemical jet milling with novel cathode tool, J. Mater. Process. Technol. 309 (2022), 117731, https://doi.org/10.1016/j.jmatprotec.2022.117731.
[38] D. Landolt, Fundamental aspects of electropolishing, Electrochim. Acta. 32 (1987) 1–11, https://doi.org/10.1016/0013-4686(87)87001-9.
[39] M. Yasuda, F. Weinberg, D. Tromans, Pitting corrosion of Al and Al-Cu single crystals, J. Electrochem. Soc. 137 (1990) 3708–3715, https://doi.org/10.1149/1.2086291.
[40] S. Moniri, H. Bale, T. Volkenandt, Y. Wang, J. Gao, T. Lu, K. Sun, R.O. Ritchie, A. J. Shahani, Multi-step crystallization of self-organized spiral eutectics, Small 16 (2020), 1906146, https://doi.org/10.1002/smll.201906146.
[41] S. van der Walt, N. Smith, MPL Colormaps, (2020). https://bids.github.io/colormap/.
[42] P. de Groot, Principles of interference microscopy for the measurement of surface topography, Adv. Opt. Photon. 7 (2015) 1, https://doi.org/10.1364/AOP.7.000001.
[43] F. Barré, J. Lopez, On a 3D extension of the MOTIF method (ISO 12085), Int. J. Mach. Tools Manuf. 41 (2001) 1873–1880, https://doi.org/10.1016/S0890-6955(01)00051-7.
[44] G. Nolze, R. Hielscher, Orientations – perfectly colored, J. Appl. Crystallogr. 49 (2016) 1786–1802, https://doi.org/10.1107/S1600576716012942.
[45] S.I. Wright, M.M. Nowell, S.P. Lindeman, P.P. Camus, M. De Graef, M.A. Jackson, Introduction and comparison of new EBSD post-processing methodologies, Ultramicroscopy 159 (2015) 81–94, https://doi.org/10.1016/j.ultramic.2015.08.001.
[46] A.S. Madhvacharyula, A.V.S. Pavan, S. Gorthi, S. Chitral, N. Venkaiah, D.V. Kiran, In Situ Detection of Welding defects: a Review, 66, Weld. World, 2022, pp. 611–628, https://doi.org/10.1007/s40194-021-01229-6.
[47] L. Wang, Y. Wei, J. Chen, W. Zhao, Macro-micro modeling and simulation on columnar grains growth in the laser welding pool of aluminum alloy, Int. J. Heat Mass Transf. 123 (2018) 826–838, https://doi.org/10.1016/j.ijheatmasstransfer.2018.03.037.
[48] S. Tang, R. Backofen, J. Wang, Y. Zhou, A. Voigt, Y.-M. Yu, Three-dimensional phase-field crystal modeling of fcc and bcc dendritic crystal growth, J. Cryst. Growth. 334 (2011) 146–152, https://doi.org/10.1016/j.jcrysgro.2011.08.027.
[49] T. DebRoy, H.L. Wei, J.S. Zuback, T. Mukherjee, J.W. Elmer, J.O. Milewski, A. M. Beese, A. Wilson-Heid, A. De, W. Zhang, Additive manufacturing of metallic components – Process, structure and properties, Prog. Mater. Sci. 92 (2018) 112–224, https://doi.org/10.1016/j.pmatsci.2017.10.001.
[50] S. Singh, Y. Guo, B. Winiarski, T.L. Burnett, P.J. Withers, M. De Graef, High resolution low kV EBSD of heavily deformed and nanocrystalline Aluminium by dictionary-based indexing, Sci. Rep. 8 (2018) 10991, https://doi.org/10.1038/s41598-018-29315-8.
[51] C. Zhu, M. Seita, A physics-based model for crystal orientation dictionary indexing by directional reflectance microscopy, Acta Mater. 231 (2022), 117863, https://doi.org/10.1016/j.actamat.2022.117863.
[52] J. Zeng, Y. Zheng, M. Rycenga, J. Tao, Z.-Y. Li, Q. Zhang, Y. Zhu, Y. Xia, Controlling the shapes of silver nanocrystals with different capping agents, J. Am. Chem. Soc. 132 (2010) 8552–8553, https://doi.org/10.1021/ja103655f.
[53] S. Bai, L. Wang, Z. Li, Y. Xiong, Facet-engineered surface and interface design of photocatalytic materials, Adv. Sci. 4 (2017), 1600216, https://doi.org/10.1002/advs.201600216.